University of South Florida
Scholar Commons

Graduate Theses and Dissertations

Graduate School

6-7-2016

Waterproofing Shape-Changing Mechanisms Using Origami Engineering; Also a Mechanical Property Evaluation Approach for Rapid Prototyping

Andrew Jason Katz
University of South Florida, andrewsky96@gmail.com

Follow this and additional works at: http://scholarcommons.usf.edu/etd

Part of the Mechanical Engineering Commons

Scholar Commons Citation

Katz, Andrew Jason, "Waterproofing Shape-Changing Mechanisms Using Origami Engineering; Also a Mechanical Property Evaluation Approach for Rapid Prototyping" (2016). *Graduate Theses and Dissertations.*
http://scholarcommons.usf.edu/etd/6271

This Thesis is brought to you for free and open access by the Graduate School at Scholar Commons. It has been accepted for inclusion in Graduate Theses and Dissertations by an authorized administrator of Scholar Commons. For more information, please contact scholarcommons@usf.edu.

المنارة للاستشارات

www.manaraa.com

Waterproofing Shape-Changing Mechanisms Using Origami Engineering; Also a Mechanical Property Evaluation Approach for Rapid Prototyping

by

Andrew J. Katz

A dissertation submitted in partial fulfillment
of the requirements for the degree of
Doctor of Philosophy in Mechanical Engineering
Department of Mechanical Engineering
College of Engineering
University of South Florida

Major Professor: Craig P. Lusk, Ph.D.
Nathan Crane, Ph.D.
Kyle Reed, Ph.D.
Yu Sun, Ph.D.
Mark Weston, M.Arch.

Date of Approval:
May 19, 2016

Keywords: Shape-Shifting, Mechanical Optimization, Compliant Mechanisms, Stiffness Testing, Strength Testing

Copyright © 2016, Andrew J. Katz

المنارة للاستشارات

www.manaraa.com

DEDICATION

I dedicate my work to my understanding wife and my supporting family.

المنارة للاستشارات

www.manaraa.com

ACKNOWLEDGMENTS

The authors of this work gratefully acknowledge the support of the National Science Foundation, Grant # CMMI-1053956.

المنارة للاستشارات

www.manaraa.com

TABLE OF CONTENTS

www.manaraa.com

المنارة للاستشارات

www.manaraa.com

LIST OF TABLES

المنارة للاستشارات

www.manaraa.com

LIST OF FIGURES

www.manaraa.com

www.manaraa.com

www.manaraa.com

ABSTRACT

My work has been focused on compliant mechanisms, origami engineering, and rapid prototyping. Two of the projects that I worked on were focused on compliant mechanisms and origami engineering. The similar goal of both of those projects was to create an origami membrane whose kinematics mimic that of an existing mechanism. The first project created an origami membrane to mimic the kinematics of a planar shape-changing mechanism. This mechanism was a square shaped unit-cell which could shear, compress, and expand in its own plane. In addition to waterproofing the mechanism, the first project also sought to optimize the dimensions of the mechanism in order to reduce internal stresses during actuation. The results of the optimization portion of this project were a reduction of internal stresses by more than 22%. The results of the origami synthesis portion of the project was the creation of a membrane with an origami pattern whose kinematics mimic that of the shape-shifting surface. The origami membrane is capable of being folded into each of the various positions that the shape-shifting surface is able to fold into. The second project sought to create a similar type of origami fold pattern, but for a Shape Morphing Space Frame (SMSF). This project created an origami membrane designed to mimic the kinematics of a mechanism that had been developed in a different previous project. The mechanism consisted of a series of Linear Bistable Elements (LBEs) which were assembled to form a cylinder. When the LBEs were actuated the cylinder would deform to a hyperboloid. This project created an origami membrane whose kinematics mimic that of the shape-morphing space frame and was able to change side length by more than 30%. The origami membrane was able to fold to each of the SMSF's states. This project also developed a method for synthesizing an origami fold pattern

المنارة للاستشارات

www.manaraa.com

with shape-morphing triangles. Both of the first two projects that comprise this dissertation sought to develop an origami fold pattern whose kinematics mimic that of an existing mechanism. In each of these projects one of the future goals for the project was to create a prototype where the mechanism and the origami are fabricated together as one integrated prototype. Possible methods of accomplishing this goal include rapid prototyping. Thus, the mechanics of rapid prototyping are of concern for future work on these projects. The third project developed a part which could be printed from a Fused Deposition Modeling (FDM) machine to test certain material properties (yield strength and elastic modulus) after it had been processed through the FDM. This would allow the material properties to be tested without the use of expensive test equipment. This project developed eight parts which could be used to bracket certain material properties of rapid prototyped parts after processing. The parts developed in this project were capable of bracketing the material properties of the materials in question, and were able to do so when tested across multiple FDM machines. The results of this work were stress-strain data which indicates the behavior of the part under load, and a method for inexpensively testing the material properties of rapid prototyped parts after processing.

المنارة للاستشارات
www.manaraa.com

CHAPTER 1: OVERVIEW

The common area of all of my research at USF has been the field of compliant mechanisms, “a compliant mechanism is one which gets some or all of its motion from deflection of flexible members” [1]. Some examples of compliant mechanisms include nail clippers, diving boards, and certain plastic bottle tops (such as shampoo bottles). My research has largely focused on shape-changing mechanisms, which use compliant mechanisms to change their shapes. I have taken certain shape-changing mechanisms and added waterproofing barriers to them in order to make them waterproof. A substantial part of my research has involved joining compliant mechanisms with novel origami membranes, to accomplish this goal.

One of the primary themes of my research has been developing solutions that involve the use of origami, in order to make a mechanism waterproof [2], [3]. The mechanisms in question are shape-changing mechanisms, which can morph from an initial state, with a specific initial geometry (i.e. square or cylindrical) to a deformed state (i.e. a different parallelogram or hyperbolic). Origami engineering is a burgeoning field of engineering that shows promise in a multitude of fields. One of the reasons that origami is becoming more common in engineering is because it offers the ability to have a high ratio of deployed volume to stowed volume. This entails that a device can be small while stowed, and substantially larger when it is deployed. This idea is particularly useful in applications where efficient use of volume is critical (i.e. the aerospace industry). Although origami has been developed for centuries, its use in engineering applications has been more heavily studied in recent years [4]-[8].

www.manaraa.com

Part of the development of origami for engineering applications has involved research on the theory and physics that govern it. There has been research pertaining to the rules for origami synthesis that must be followed in order for a fold pattern to be feasible [9]-[11], as well as projects which describe the mobility of various origami designs [12]. In addition to the work described in this dissertation, there has been other work that combines the fields of origami and compliant mechanisms [13], [14]. Several projects have studied the use of computational methods for developing algorithms to generate origami solutions [11], [15]-[18]. There have also been projects which served to develop actuation methods for origami [19]-[23], as well as sensing methods [24]. Paper is a good material for use in prototyping origami but in applications, other materials are often required. For this reason there has been research into ways of producing certain fold types in materials that do not yield the way paper does when folded [25], [26]. There have also been projects that perform Finite Element Analysis (FEA) on origami [23], [27]. In addition there has been extensive research devoted to developing solutions for origami to be used in specific applications. Origami has been used to optimize raised floor structures [28]. It has also been used by the U.S. military for portable shelters [29], and to make lithium-ion batteries [30]. It has been considered for car bumpers for its potential to absorb energy [31], [32], as well as in robotics and electronics applications [33], [34].

The development of origami analysis methods involves creating novel models for describing the behavior of origami. It is often helpful to model origami as rigid mechanisms using mechanism theory [35], [36]. It is also beneficial to understand graph theory for the purpose of modeling the behavior and structure of origami [37]-[41].

There has been past research pertaining to shape-changing mechanisms [42]-[46], as well as topology optimization and synthesis [20], [46]-[49]. There has also been previous research on

المنارة للاستشارات
www.manaraa.com

waterproofing and the various methods for accomplishing it, such as the use of labyrinth seals [50]-[56], and also other seals [57], [58]. Other projects have sought to optimize various properties of compliant mechanisms one example of which is weight [59]-[60].

Chapter 4 of my dissertation is based on the development of a simplified method for testing the properties of materials that have been processed through a rapid prototyper. One of the most popular rapid prototyping methods is Fused Deposition Modeling (FDM). This method involves heating the feed-stock material to a high temperature so that it becomes soft enough to extrude. After which it is cooled back to room temperature and it hardens. Given the thermal cycling involved in this process, and the change in geometry from a reasonably homogenous block of material to a matrix of stacked, extruded material, the material properties of the feed stock can change in unpredictable ways. Thus, testing FDM parts after processing can be an important part of the design process. One common method of testing material properties involves the use of test equipment, some of which can be large and expensive. Thus, developing a simplified and inexpensive method for testing material properties after proccessing would be particularly beneficial to home users.

Other research has similarly develped alternative test methods for testing mechanical properties of materials [61]. There has also been previous research into the mechanical properties of additive manufactured parts [62], [63]. As well as other research into improving the microstructure of additive manufactured parts [64]. One aspect of this project was controlling the effects of stress concentrations at the base of a cantilever beam, other projects have similarly considered these types of effects [65].

In Chapter 2 of the dissertation I discuss a project in which a shape-shifting surface was made waterproof by adding a flexible origami membrane whose kinematics mimic that of the

www.manaraa.com

underlying mechanism. The mechanism in this project was a square shaped, planar mechanism which could compress to a smaller square, expand to a larger square, and shear to a rhombus-like shape. In Chapter 3 I discuss a similar project, which took a shape-morphing space frame and made it waterproof, also by adding a flexible origami membrane whose kinematics mimic that of the underlying mechanism. In this project the mechanism was initially a cylinder, which when deformed, became a hyperboloid. In Chapter 4 I discuss a project which sought to develop a rapid, inexpensive test method for testing parts that were made by rapid prototyping. In this project the goal was to develop a test method that did not require the use of expensive test equipment.

المنارة للاستشارات

www.manaraa.com

CHAPTER 2: DESIGN AND KINEMATIC OPTIMIZATION OF A WATERPROOF SHAPE-SHIFTING SURFACE (SSS)

Portions of Chapter 2 were previously published in Proceedings of the ASME International Design Engineering Technical Conference & Computers and Information in Engineering Conference in 2015 and has been reproduced with permission from ASME. I (Andrew Katz) was the first author, and my advisor Dr. Craig Lusk was the second author [2].

2.1 Introduction

The objective of this Chapter is to design and optimize a waterproof shape-shifting surface. A shape-shifting surface [66] is a surface which maintains its effectiveness as a physical barrier while changing its shape. One way of achieving this is using arrays of multilayered unit cells. The unit cell (Figure 1 shows its equilibrium position), used in this Chapter, is a square which can compress to two-thirds of its original size, expand in tension to four-thirds of its original size, or shear +/- 30 degrees at each corner while maintaining integrity. Compression or expansion can occur in the *X* and/or *Y* direction(s). Previous designs acted as "line-of-sight" barriers but had gaps which would allow for fluid flow between layers [66].

A waterproof shape-shifting surface's benefit would lie in its ability to preserve structural integrity in the surface's normal direction and allow shape changing in the surface. This stiffness anisotropy (flexible in-plane, stiff normal to the plane) is provided by the SSS's novel geometry and is in contrast to the typical behavior of isotropic homogeneous surfaces, which are typically

Copyright by ASME, Andrew J. Katz; Craig P. Lusk, Paper Number DETC2015-47595

المنارة للاستشارات

www.manaraa.com

much stiffer in-plane. Our goal was to combine the structural integrity of a shape-shifting surface with the water-tight seal of a flexible plastic sheet to create a surface which would be strong, flexible, and waterproof.

A waterproof shape-shifting surface could have applications in the maritime and medical industries. In the maritime industry the device could serve to prevent spilled fluid, such as oil from spreading further into a body of water. In the medical industry it could act as a sterile barrier either to protect caregivers from a quarantined patient, or to protect immuno-compromised patients from infection. In these applications, such surfaces may have advantages of allowing greater ranges of motion or greater energy absorption capability (stored elastic potential in compliant members) than existing surfaces, which could be important in dealing with fluids under pressure.

The first goal of the current project was to make the unit cell waterproof i.e. an effective barrier to fluid flow normal to the surface. The second goal was to optimize the geometry of the compliant link to minimize internal stresses when unit cells deforms. The device was made waterproof by adding a thin flexible membrane between the layers. The membrane was designed to have an origami fold pattern which would allow it to have the same kinematics as the device. The structural integrity was improved by creating an optimization routine which minimized internal stress when the device is actuated.

Copyright by ASME, Andrew J. Katz; Craig P. Lusk, Paper Number DETC2015-47595

المنارة للاستشارات
www.manaraa.com

2.1.1 Background

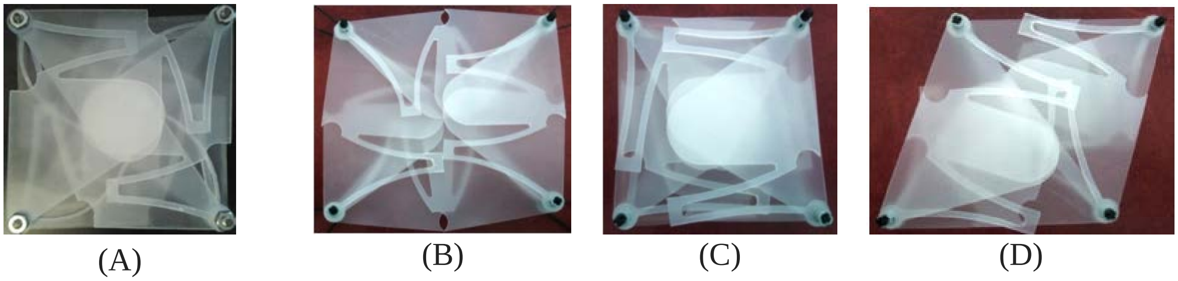
(A) (B) (C) (D)

Figure 1 The unit cell in its equilibrium position (A), expanded position (B), compressed position (C), and its sheared position (D)

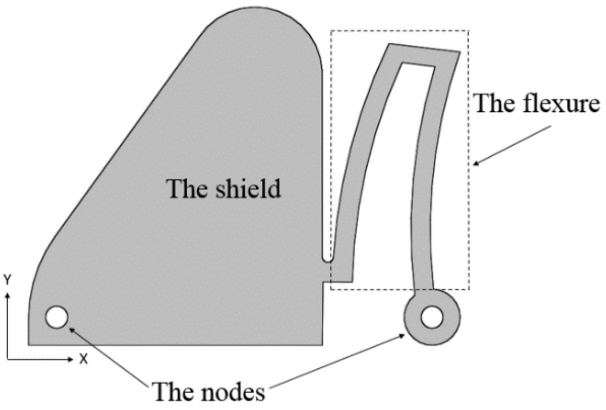

Figure 2 Labeled example of our initial link design

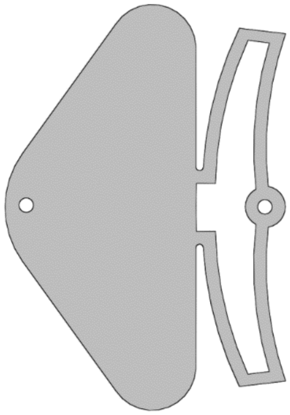

Figure 3 Example of the double-size initial part

The compliant links are the individual pieces which makeup the device, an example is shown in Figure 2, which is labeled to show its various components and the coordinate system orientation. The out-of-the-page direction is aligned with the *Z*-axis. The axis-orientation is the same for all figures. When two unit cells are adjacent to one another, the part shown in Figure 2 would be adjacent to a similar part with a mirrored orientation. When two parts meet like that, they can be individual, they can be hinged (or connected), or they can be fused (as shown in Figure 3). When the parts are fused, compression and tension in the flexure occurs if the path of the node is

www.manaraa.com

not a straight line in the *X*-direction. Thus, the kinematics of the moving node are a significant determiner of the maximum stresses seen as the flexure deflects.

The initial design of the SSS is described in [66]. A pseudo-rigid-body model (PRBM) [1] was used to represent the SSS link as a system of rigid links connected by torsional springs. Solid mechanics theory was used to analyze the behavior of the part using the virtual work method. Together these theories form the basis for the optimization component of the project, which aimed to reduce the stress in the flexure by improving its kinematics (i.e. making its motion more nearly straight-line in the *X*-direction).

The PRBM is a way of modeling a compliant mechanism with a good degree of accuracy when large deflections are going to occur. When a device is going to undergo small deflections, the small angle approximation can be used, where $\sin(\theta) \cong \theta$. When the deflection is large enough that this approximation is no longer a reasonable assumption, a different method is required. The method used in this project was the PRBM, where compliant segments are modeled as two rigid members connected by a torsional spring.

The principle of virtual work involves using a virtual deflection of a member to measure the amount of work done in order to make a member deflect. This allows us to calculate the change in potential energy of a series of springs (such as the ones used in the PRBM).

Previous papers have analyzed methods for synthesizing origami patterns for various purposes [67], [68]. Other papers focused on design of origami fold patterns based on a series of constraints. While some origami papers have focused on optimization [68], [69], and some on minimizing out-of-plane thickness [70], and other papers that were useful to this project simply focused on a variety of considerations when engineering origami such as crease characterization

Copyright by ASME, Andrew J. Katz; Craig P. Lusk, Paper Number DETC2015-47595

www.manaraa.com

[71]. Another paper that discussed optimization of compliant mechanisms was [72], which also used two nested routines to optimize a compliant mechanism.

2.1.2 Overview

Chapter 2 focuses on the design of the SSS and the origami membrane that makes it waterproof. It first discusses the optimization of the compliant link of the surface and the modeling that allowed the link to be optimized. Section 3 discusses the origami membrane and how it was designed so that its kinematics mimic the kinematics of the SSS unit cell. Section 4 has the conclusions and reviews the contributions of the Chapter and the plans for future work.

2.2 Kinematic Optimization

When the unit cell is compressed or expanded, the node attached to the compliant arm tends to move in an arc-shaped path. This indicates that in the double-size version, when the arm is forced to move in a straight line, there will be internal stresses in the compliant arm associated with it moving on a different path. Optimizing the kinematics of the compliant link, making its motion tend to a straight-line, minimizes these internal stresses, thus making a more efficient design. The optimization was based on the initial model shown in Figure 4.

To begin the optimization, a PRBM of the compliant link was constructed, and a vector loop was drawn [1], as shown in Figure 4. The dotted circles at the tips of vectors $\vec{r_1}, \vec{r_2}, \vec{r_3}$, and $\vec{r_4}$ indicate the positions of the torsional springs in the PRBM.

Copyright by ASME, Andrew J. Katz; Craig P. Lusk, Paper Number DETC2015-47595

www.manaraa.com

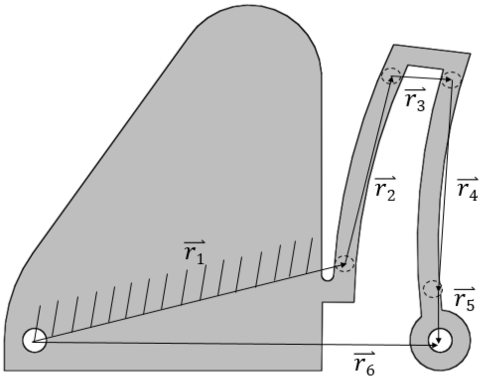

Figure 4 Vector loop of the pseudo-rigid-body model of the compliant link

The vector loop equation in the *X*-direction is:

$$r_1 cos\theta_{10} + r_2 cos\theta_{20} + \mathrm{r}_3 cos\theta_{30} + r_4 cos\theta_{40} + r_5 cos\theta_{50} = 1 \tag{1}$$

and the vector loop equation in the *Y*-direction is:

$$r_1 sin\theta_{10} + r_2 sin\theta_{20} + r_3 sin\theta_{30} + r_4 sin\theta_{40} + r_5 sin\theta_{50} = 0 \tag{2}$$

where r_{1-5} are the lengths of each link of the vectors, and the thetas are the initial angles of the members, measured counter-clockwise positive from the *X*-axis, at the tail of the respective vectors. The optimization variables are the position coordinates x_1, x_2, x_3, y_1, y_2, y_3, and y_4. The coordinates are the tips of their respective vectors. The virtual work is then calculated using the equation:

$$\vec{F}_y \cdot \delta\vec{z}_2 + \vec{F}_x \cdot \delta\vec{z}_1 - \Sigma \frac{\delta V}{\delta q_i} \delta q_i = 0 \tag{3}$$

where $\vec{F}_x$ is the applied force which contributes to expansion or compression of the unit cell, and $\vec{F}_y$ is the internal force that causes tension or compression in the double-size version. The $d\vec{z}$ vectors are displacement vectors, *V* is potential energy from springs, and the *q* variables are the generalized position coordinates.

Copyright by ASME, Andrew J. Katz; Craig P. Lusk, Paper Number DETC2015-47595

www.manaraa.com

$$q_1 = r_6 \tag{4}$$

$$q_2 = r_5 \tag{5}$$

$$q_3 = \theta_2 \tag{6}$$

$$\overrightarrow{z_1} = r_6 \tag{7}$$

$$\overrightarrow{z_2} = r_6 + ir_5 \tag{8}$$

$$\delta\overrightarrow{z_1} = \delta r_6 \tag{9}$$

$$\delta\overrightarrow{z_2} = \delta r_6 + i\delta r_5 \tag{10}$$

Vector r_6 remains horizontal, and fixed at the tail. The compliance of the members is modeled by the aforementioned torsional springs located at the tips of $\overrightarrow{r_1}, \overrightarrow{r_2}, \overrightarrow{r_3},$ and $\overrightarrow{r_4}$. The equation for the potential energy in all of the torsional springs is then:

$$V = \frac{1}{2}K_2\Psi_2^2 + \frac{1}{2}K_3\Psi_3^2 + \frac{1}{2}K_4\Psi_4^2 + \frac{1}{2}K_5\Psi_5^2 \tag{11}$$

where the K variables are the spring constants of the torsional springs, and

$$\Psi_2 = (\theta_2 - \theta_{20}) - (\theta_1 - \theta_{10}) \tag{12}$$

$$\Psi_3 = (\theta_3 - \theta_{30}) - (\theta_2 - \theta_{20}) \tag{13}$$

$$\Psi_4 = (\theta_4 - \theta_{40}) - (\theta_3 - \theta_{30}) \tag{14}$$

$$\Psi_5 = (\theta_5 - \theta_{50}) - (\theta_4 - \theta_{40}). \tag{15}$$

To solve equation (3), it is first written using each of the three *q* variables. Equation (11) is then differentiated with respect to each of the three *q* variables so that it can be plugged into equation (3). The results are:

$$F_x = \frac{dV}{dr_6} \tag{16}$$

Copyright by ASME, Andrew J. Katz; Craig P. Lusk, Paper Number DETC2015-47595

www.manaraa.com

$$F_y = \frac{dV}{dr_5} \tag{17}$$

$$\frac{dV}{d\theta_2} = 0 \tag{18}$$

$$\frac{dV}{dr_6} = k_3\Psi_3\frac{d\Psi_3}{dr_6} + k_4\Psi_4\frac{d\Psi_4}{dr_6} + k_5\Psi_5\frac{d\Psi_5}{dr_6}. \tag{19}$$

To solve equations (16) – (19), kinematic equations are used to find expressions for $\frac{dV}{d\vec{r}_6}, \frac{dV}{dr_5}$, and $\frac{dV}{d\theta_2}$. We use equations (1) and (2) in complex form:

$$\vec{x} = r_1 e^{i\theta_{10}} + r_2 e^{i\theta_2} + r_3 e^{i\theta_3} + r_4 e^{i\theta_4} + r_5 e^{i\theta_5} \tag{20}$$

Equation (20) is then differentiated with respect to r_6 and rearranged to yield:

$$\frac{d\theta_4}{dr_6} = \frac{cos\theta_3}{r_4\sin(\theta_4 - \theta_3)}. \tag{21}$$

The same process can then be applied to solve for $\frac{d\theta_3}{dr_6}$. Once those coefficients have been obtained, the final equation for this part of the calculations is produced:

$$F_x = \frac{1}{\sin(\theta_3 - \theta_4)}\left[\frac{-k_3\Psi_3 cos\theta_4}{r_3} + \frac{k_4\Psi_4 cos\theta_3}{r_4} + \frac{k_4\Psi_4 cos\theta_4}{r_3} + \frac{k_5\Psi_5 cos\theta_3}{r_4}\right]. \tag{22}$$

The same process is then used to solve for F_y and $\frac{dV}{d\theta_2}$. Once these equations have been solved they become the basis for the optimization program.

$$F_y = \frac{1}{\sin(\theta_3 - \theta_4)}\left[\frac{k_3\Psi_3}{r_3}\cos(\theta_5 - \theta_4) - k_4\Psi_4\left(\frac{\cos(\theta_5 - \theta_3)}{r_4} + \frac{\cos(\theta_5 - \theta_4)}{r_3}\right) - \frac{k_5\Psi_5}{r_4}\cos(\theta_5 - \theta_3)\right] \tag{23}$$

www.manaraa.com

$$\frac{dV}{d\theta_2} = k_2\Psi_2 + k_3\Psi_3\left[\frac{-r_2\sin(\theta_2-\theta_4)}{r_3\sin(\theta_3-\theta_4)} - 1\right] + \left[\frac{-k_4\Psi_4 r_2\sin(\theta_2-\theta_3)}{r_4\sin(\theta_4-\theta_3)}\right] + \left[\frac{k_4\Psi_4 r_2\sin(\theta_2-\theta_4)}{r_3\sin(\theta_3-\theta_4)}\right] + \left[\frac{-k_5\Psi_5 r_2\sin(\theta_2-\theta_3)}{r_4\sin(\theta_4-\theta_3)}\right] = 0 \tag{24}$$

An optimization program was written in MATLAB® and works in two phases. In the first phase, it solves for five unknown variables using five equations. The five equations are equations 1, 2, and 22 - 24. The five unknown variables are F_x, F_y, θ_2, θ_3, and θ_4. Our routine solves the equations using the *fsolve* command, a gradient-based optimization which searches for the root(s) of a system of equations. The initial guess values were based on an existing prototype of the compliant link. The unknowns are found for the feasible range of input values of r_6. The most important output of the first phase of the program is the maximum force experienced in the *Y*-direction (our internal stress metric).

The second phase of the optimization uses the *fmincon* command (a gradient-based optimization routine) to minimizing the maximum force experienced by the compliant arm in the *Y*-direction. In this phase, the program repositions the coordinates that form the members of the pseudo-rigid-body model, then re-determines the maximum force in the *Y*-direction. It repeats this process, searching for coordinate values which minimize the force in the *Y*-direction. The stopping criteria for the function value is 10^{-6} (i.e. practically zero). The constraints of the program are:

1. The beginning and end of the vector loop cannot change position. So the tail of $\overrightarrow{r_1}$ and the tip of $\overrightarrow{r_5}$ do not change position, and $\overrightarrow{r_6}$ remains horizontal.
2. Vector $\overrightarrow{r_5}$ must remain vertical. This is based on the symmetry of the double-size model.

In order to ensure that the solution which the program found was the best solution, several forms of the optimization were run. First, a gradient-based routine (*fmincon*) with initial values

Copyright by ASME, Andrew J. Katz; Craig P. Lusk, Paper Number DETC2015-47595

www.manaraa.com

taken from an existing prototype was used, then MultiStart (MS) and GlobalSearch (GS) optimizations were also run, which also use the *fmincon* routine, but have different methods for generating initial values. The *fmincon* optimization uses a prescribed set of initial values to plug into the objective function. The MultiStart routine generates a defined number of sets of initial values randomly, then runs each of them, searching for the optima, the MultiStart used in this program used twenty sets of initial values. The GlobalSearch (GS) routine starts with a prescribed set of initial values, then generates additional sets of initial values using a scoring system to determine which initial values are most likely to give optimal results [73]. The GlobalSearch routine found the solution which was determined to be the best. This determination was based on the objective function value. The coordinates which the program determined were optimal, formed the basis for the new designs of the compliant link.

2.2.1 Optimization Results

Table 1 Optimized vectors

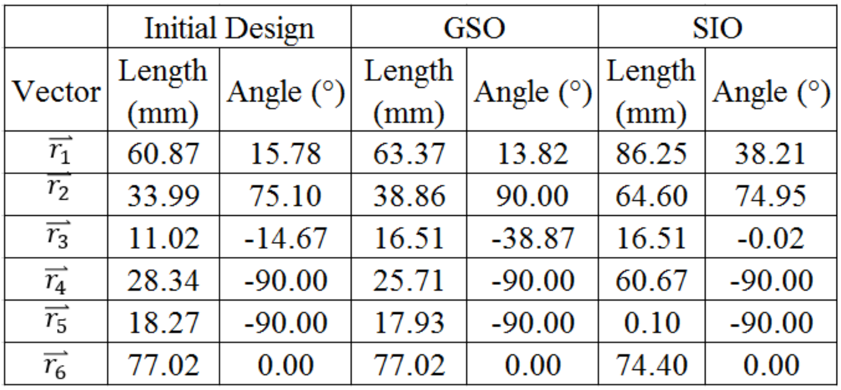

	Initial Design		GSO		SIO	
Vector	Length (mm)	Angle (°)	Length (mm)	Angle (°)	Length (mm)	Angle (°)
$\vec{r_1}$	60.87	15.78	63.37	13.82	86.25	38.21
$\vec{r_2}$	33.99	75.10	38.86	90.00	64.60	74.95
$\vec{r_3}$	11.02	-14.67	16.51	-38.87	16.51	-0.02
$\vec{r_4}$	28.34	-90.00	25.71	-90.00	60.67	-90.00
$\vec{r_5}$	18.27	-90.00	17.93	-90.00	0.10	-90.00
$\vec{r_6}$	77.02	0.00	77.02	0.00	74.40	0.00

The output of the optimization program was a set of coordinates that form a vector loop. The coordinates have been converted to vector form and are shown in Table 1. In Table 1 and

Copyright by ASME, Andrew J. Katz; Craig P. Lusk, Paper Number DETC2015-47595

www.manaraa.com

Table 2 GSO indicates the GlobalSearch Optimized compliant link, and SIO indicates the Simple Optimized compliant link. The loop must then be interpreted to form a three-dimensional part. One limitation of our process was that the interpretation of the vector loop as a compliant mechanism is under determined and a variety of compliant links might be equivalent the PRBM. Thus, this kinematic optimization is not as definitive as perhaps some forms of topology optimization might be. The optimized version of the compliant link is shown in Figure 5. Comparing Figures 4 and 5 shows that the optimization program determined that changing the geometry of the flexure of the compliant link would reduce the internal stresses during operation.

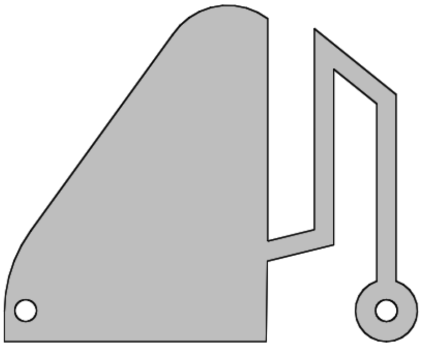

Figure 5 Drawing of the optimized compliant link

Finite Element Analysis (FEA) performed using SolidWorks® showed a 22.91% reduction in the maximum Von Mises stress experienced by the compliant link during operation as shown in Table 2. This analysis used polypropylene copolymer as the material. All FEA results are based on the double-size model because the double-size model was expected to experience higher stresses.

Copyright by ASME, Andrew J. Katz; Craig P. Lusk, Paper Number DETC2015-47595

www.manaraa.com

Table 2 Results from FEA and optimization

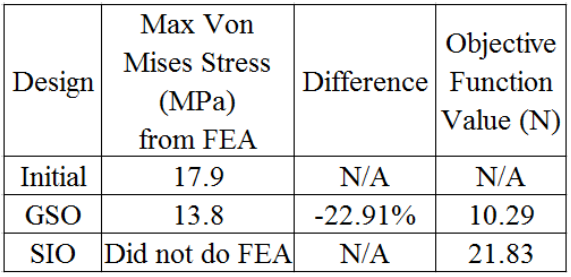

Design	Max Von Mises Stress (MPa) from FEA	Difference	Objective Function Value (N)
Initial	17.9	N/A	N/A
GSO	13.8	-22.91%	10.29
SIO	Did not do FEA	N/A	21.83

2.3 Origami Design

For this project the chosen method of making the unit cell waterproof was adding a piece of flexible material or ‘membrane’ with an origami fold pattern between the layers of the unit cell. This piece of material is henceforth referred to as ‘the membrane’. For initial prototyping, the membrane was made out of standard printer paper. The fold pattern was designed so that its kinematics would match the kinematics of the unit cell. A simplified model of the shields (shown in Figure 6) was used for the origami design, where each triangle represents one shield. It is simplified because this model of the shields does not include the flexure portion of the links (shown in Figure 2). In this model, each shield exists on a different level in the *Z*-axis, where the *Z*-axis is into/out of the page. The design of the fold pattern was divided into three parts: edges, which allow for compression and expansion of the unit cell; corners, which allow shearing of the unit cell, and a center piece which provides a contiguous (and hence waterproof) surface and allows center motion.

Copyright by ASME, Andrew J. Katz; Craig P. Lusk, Paper Number DETC2015-47595

www.manaraa.com

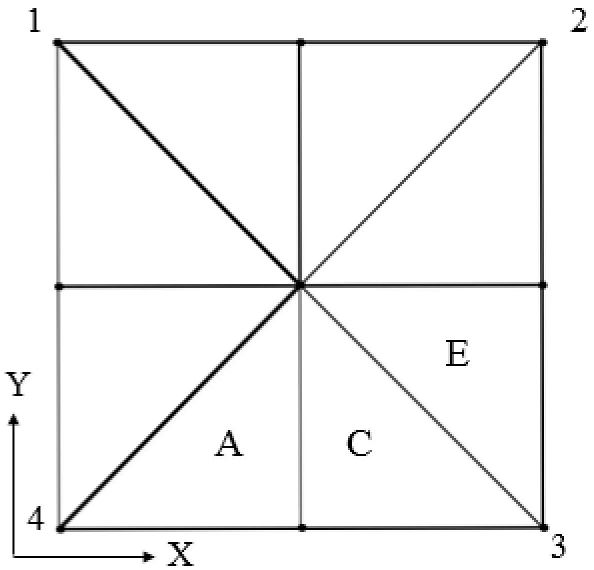

Figure 6 Simplified model of the unit cell, with the nodes numbered and certain shields designated with letters

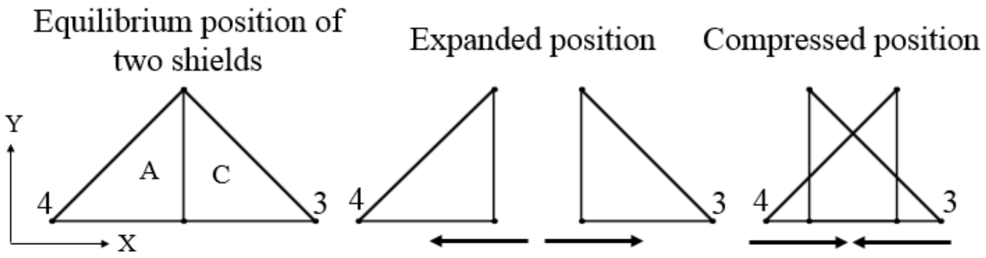

Figure 7 Diagram of relative translation between two shields sharing a side, which provides for compression/expansion of the unit cell.

As shown in Figure 7, two adjacent shields on a side may be either pulled apart in tension, or pushed together in compression. Thus the origami membrane that connects the two shields on a side must fold in a way that permits this relative translation. Rotational motion (shown in Figure 8) at the corners of the unit cell permits it to shear. The rotations that occur during shear are of course coupled. For example, if the angle at nodes 2 and 4 become more acute, then the angles at nodes 1 and 3 become more obtuse, and the part of the origami membrane at each of the corners would need to fold in ways that permit both acute and obtuse angles at each corner.. Based on the

Copyright by ASME, Andrew J. Katz; Craig P. Lusk, Paper Number DETC2015-47595

www.manaraa.com

constraints of the unit cell it was determined that two shields at a node would need to be able to rotate up to thirty degrees (positive and negative) with respect to one another.

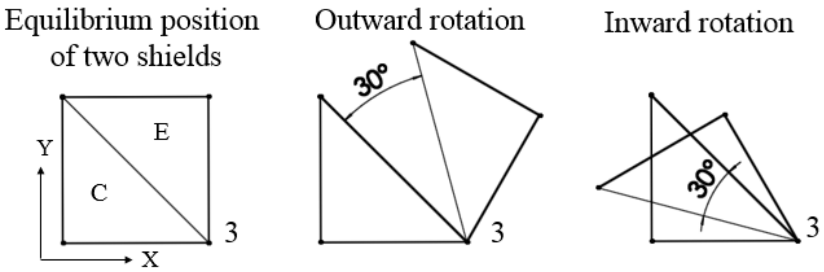

Figure 8 Diagram of the rotational motion of two shields

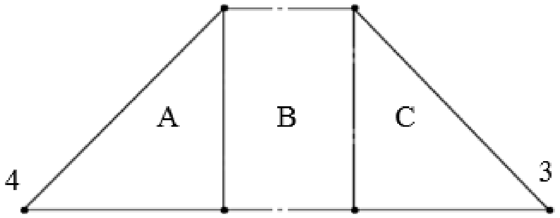

Figure 9 Schematic of the edge piece of the origami membrane

As previously stated, the unit cell was designed to expand to four-thirds of its original side length, and compress to two-thirds of its original side length, where the original side length was three inches. For this reason, the portion of the origami membrane that connects two adjacent shields needed to be one inch. Given that shields that are connected at a node need to be able to rotate up to thirty degrees (positive or negative) with respect to one another, the portion of the membrane that connects these shields (which originates along the hypotenuses of the triangles) needed to be thirty degrees wide. The design for the portion of the origami membrane that allows compression/expansion (shown in Figure 7) is the same on each edge of the unit cell.

www.manaraa.com

In Figure 9, the triangles are the same adjacent shields shown in Figure 7. A membrane (labeled ‘B’) connects the two shields and fills the gap as the shields move relative to one another.

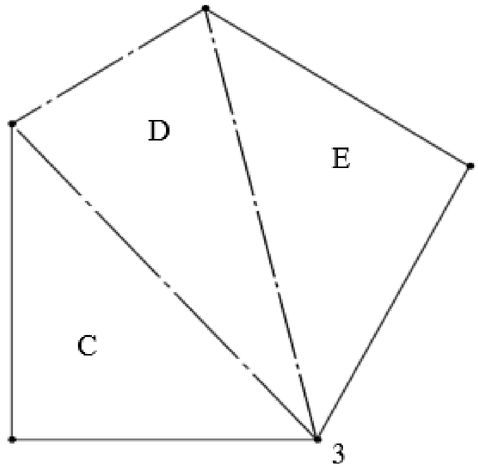

Figure 10 Schematic of the corner pieces of the origami membrane

Figure 10 shows the origami sections that connect the corner pieces. The right triangles on the left and right (sections C and E) are the shields which are the same as the respective ones shown in Figure 8. Node 3 is also the same as in Figure 8. Section D in Figure 10 is analogous to section B in Figure 9, in that it is the membrane section which fills the gaps between shields as the corners shear.

The edge and corner pieces of the origami connect to one another in series going around the outside perimeter of the unit cell. These pieces seal the gaps between the shields and prevent fluid from flowing between them. Since these pieces are wrapped around the outer edges and corners of the unit cell, they leave a gap in the middle of the unit cell, where fluid would be able to flow. The edge and corner parts of the origami design were relatively simple because they are each only concerned with the relative motion of two shields. When four sections such as the one shown in Figure 9 are arranged in a square to form part of the origami membrane the drawing

Copyright by ASME, Andrew J. Katz; Craig P. Lusk, Paper Number DETC2015-47595

www.manaraa.com

shown in Figure 12 is generated. In Figure 12, the shield sections (like those labeled C and E in Figure 10) are colored black, while the membrane is left white. Four additional triangles (labeled I, II, III, and IV) are added to each corner of the membrane in order to have a geometry that is planar, i.e. capable of being cut from a flat sheet of material. In use, section I would be permanently bonded to II, and III to IV, resulting in a corner that looks like Figure 10, with the additional material included (sections I, II, III and IV) becoming flaps folded under the membrane. This forces the originally planar piece of origami to fold out-of-plane, into a bowl-like shape. The membrane is then able to take on a range of positions of the unit cell, as well as expand and compress. Three positions which demonstrate the shear capacity of the membrane are: sheared to the right (shown in Figure 11), unit cell equilibrium (Figure 6), and sheared to the left (the mirror image about the *Y*-axis of Figure 11). The unit cell equilibrium (where the flexures are unstressed) is the position half way between the two sheared positions. When the unit cell is in its equilibrium position, the four arms of the star are folded in half about their center axes.

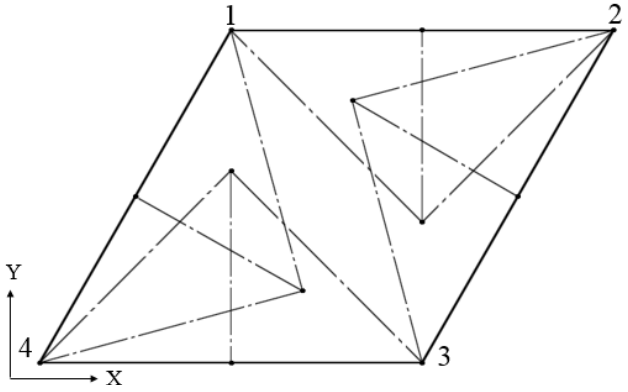

Figure 11 Unit cell in sheared position, the dotted lines show the positions of the eight shields

Copyright by ASME, Andrew J. Katz; Craig P. Lusk, Paper Number DETC2015-47595

www.manaraa.com

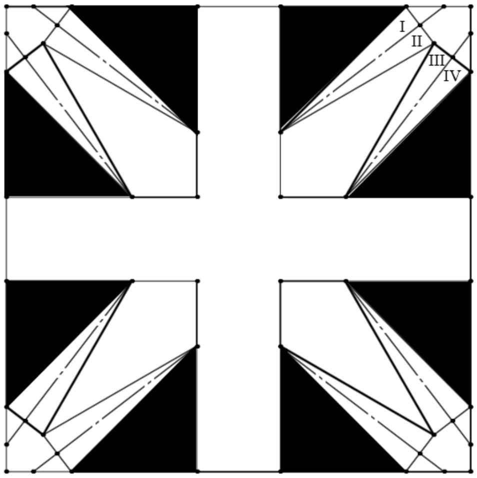

Figure 12 The perimeter of the origami membrane with fold lines that permit tension/compression and shearing of the unit cell.

The portion of the origami membrane that resides in the center of the unit cell is a more complex piece. Its complexity comes from the fact that it is concerned with the motion of eight shields. The requirements for the center of the membrane are that it does not interfere with the motion of the edges and that it satisfies the requirement that origami fold patterns be two-colorable. The fold pattern shown in Figure 13 satisfies these requirements.

Appropriate dimensions were determined based on the dimensions of the edge and corner pieces. The combination of sections V and VI in Figure 13 is similar to section D in Figure 10 but in a mirrored orientation. The design of Figure 13 is essentially four corner pieces (such as the one shown in Figure 10) connected to four edge pieces (such as the one shown in Figure 9), with a diamond fold structure in the middle of it.

Copyright by ASME, Andrew J. Katz; Craig P. Lusk, Paper Number DETC2015-47595

المنارة للاستشارات
www.manaraa.com

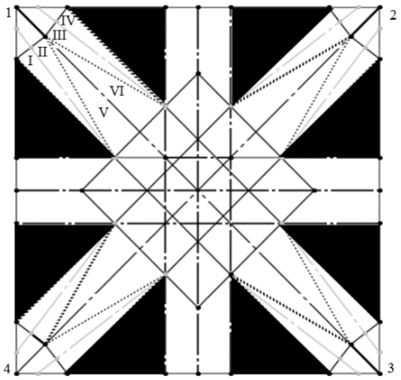

Figure 13 Schematic of the center piece of the origami membrane

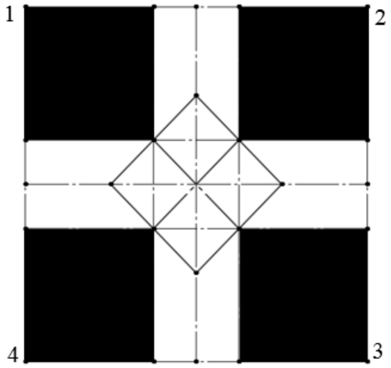

Figure 14 The border of the origami piece with the corners collapsed, and the edges expanded

The three hashed lines that run horizontal and vertical in Figure 13 are fold lines. The sections which are enclosed by those lines allow the membrane to expand in the *X* and/or *Y*-direction(s). The solid lines which form diamonds in the center of the figure are fold lines which allow the membrane to fold into the shear positions.

When the corners and edges are all brought together, the way they are in the equilibrium position, the membrane would look the same as the equilibrium position shown in Figure 6. When the corners are brought together but the edges are not, it appears the way it does in Figure 14. Note that in this context, expanded means that the membrane material between two adjacent shields

Copyright by ASME, Andrew J. Katz; Craig P. Lusk, Paper Number DETC2015-47595

www.manaraa.com

(section B of Figure 9) is expanded in tension, and collapsed means that the edges of two adjacent shields are brought together, and the membrane material between them (section D of Figure 10) is folded over.

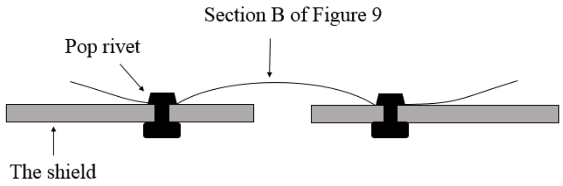

Figure 15 Side view of two adjacent shields, showing how the origami membrane mounts to them

As previously stated, the unit cell is designed to be able to expand or contract in the *X* and/or *Y*-direction(s). The design allows the unit cell to expand one inch in the *X*-direction and/or one inch in the *Y*-direction. Part of the integration of the origami membrane was attaching the origami membrane to the unit cell. The chosen method of attaching the membrane to the shields was pop rivets. Figure 15 is not to scale, section B would be one inch long.

2.3.1 Origami Results

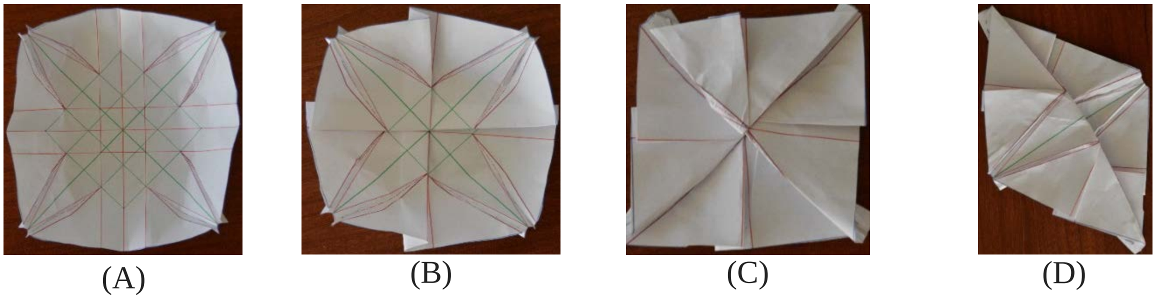
(A) (B) (C) (D)

Figure 16 The printed prototype of the origami membrane

www.manaraa.com

Figure 16A shows the origami membrane with certain sections bound (from Figure 12, section I bound to II and section III bound to IV, as described previously), but all other sections expanded. Figure 16B shows the origami in its fully compressed position. Figure 16C shows it in the equilibrium position (half way between the two shear positions), and Figure 16D shows it in the shear position. Currently, operating the membrane requires a fair amount of manipulation. One of the plans for future work is in making the operation processes simpler.

2.4 Conclusion

A design has been presented which combines the strength of solid parts with the waterproof seal and flexibility of a flexible membrane, thus creating a waterproof barrier which could potentially be used to separate fluids in a body of water. The optimization of the compliant link achieved a reduction of internal stress during operation. This type of device could have applications in the maritime industry for separating a spilled fluid from another fluid such as a body of water, or also in the medical industry to separate a sterile area from a non-sterile area. Future plans for this project are a test with a waterproof membrane, with appropriately located connectors between the shields and the membrane, allowing for controlled manipulation of the membrane.

Copyright by ASME, Andrew J. Katz; Craig P. Lusk, Paper Number DETC2015-47595

www.manaraa.com

CHAPTER 3: DESIGN OF AN ORIGAMI FOLD PATTERN FOR SHAPE-MORPHING TRIANGLES

Portions of Chapter 3 are currently in the publication process by ASME. Publication and ASME copyright pending presentation at the ASME IDETC2016 conference, August 21-24, 2016, Charlotte, NC. This content is reproduced with permission from ASME. I (Andrew Katz) was the first author, and my advisor Dr. Craig Lusk was the second author [2].

3.1 Introduction

There are two fundamental goals to this project. The first objective is to design an origami fold pattern whose kinematics mimic the kinematics of an existing bistable shape-morphing mechanism [75]. The second objective is to find a general method using origami, for morphing one triangle into another. Many shapes can be approximated by tessellating their surfaces with triangles. Morphing one shape into another can conceivably be accomplished by morphing the triangles from one shape, into the triangles that tessellate the other shape.

Possible applications for this technology could be found in multiple types of machinery. In our example the original mechanism is in the shape of a cylinder, therefor it could potentially be used as a pipe. Given its ability to change shape (go from cylindrical to hyperbolic), it could be used to change the amount of fluid flowing into a system. An example of which would be to adjust the amount of airflow being let into an engine.

المنارة للاستشارات

www.manaraa.com

The scope of the project is to create a fold pattern for a piece of origami that would be able to change shape in the same way that the existing shape morphing mechanism does. Included in the scope is to demonstrate that the method for creating this type of origami pattern is general, i.e. applicable for different dimensions.

(A) (B)

Figure 17 The mechanism in the undeformed state (A), which forms a cylinder, and the deformed state (B), which forms a hyperboloid. Adapted from [75].

This project was based on an existing design for a shape-morphing mechanism, made of Linear Bistable Elements (LBEs) [75]. This mechanism consisted of a series of unit cells, in the shape of strips of triangles. Each strip is comprised of eight triangles oriented to form a vertical rectangle. When oriented around a center, the strips formed a cylinder as shown in Figure 17A. During actuation the linear bistable elements used to form the unit cell get shorter. By actuating the bistable elements, the strips shrink, thus morphing the cylinder into a hyperboloid as shown in Figure 17B. The two stable states of the mechanism will be referred to as the undeformed and deformed states. The undeformed state refers to when the LBEs are in their extended position. In the undeformed state, the triangles that form the unit cell are all right isosceles triangles. The

المنارة للاستشارات

www.manaraa.com

deformed state refers to when the LBEs are in the shorter, contracted position. In this position, the triangles become scalene.

The purpose of a foldable origami piece with similar kinematics to that of the mechanism, is that if it were made of a waterproof material then it could serve as a waterproof membrane to the mechanism. This would result in a waterproof membrane which would move in the same way as the mechanism itself. The concept of a waterproof origami membrane was presented in a previous paper [2] for a shape-morphing mechanism which was square instead of triangular.

3.1.1 Background

A bistable mechanism is a mechanism which has two stable energy states. These are states in which the mechanism does not tend to change its position or shape [1]. The two stable states of our group's shape-morphing mechanism are an undeformed state, in which the mechanism is a cylinder, and a deformed state, in which the mechanism becomes a hyperboloid. In both states the cylinder is open ended. The mechanism is made of a series of linear bistable elements. There are four unique LBEs. One of the LBEs is shown in Figure 18.

Figure 18 Example of one of the linear bistable elements. Adapted from [75].

To design the origami fold pattern, the mechanism was discretized into a series of ten unit strips of LBEs assembled around one another to form a cylinder.

www.manaraa.com

(A) (B)

Figure 19 (A) is the undeformed unit strip, (B) is the deformed unit strip. Adapted from [75].

The unit strips are then further divided into eight triangles, four of which are unique, the other four are mirror images of the first four. The geometry in Figure 19 is simplified as a series of triangles, seen in Figure 20. The origami is then designed based on the unique four triangles henceforth referred to as the *major* triangles, which each have an undeformed and a deformed state.

(A) (B)

Figure 20 Simplified model of the unit strips. (A) is undeformed and (B) is deformed.

In their deformed states, each of the four triangles are unique. In their undeformed states they are all identical right isosceles triangles. It is also worth noting that in the deformed state, the

www.manaraa.com

number 1 triangle is isosceles, while the 2, 3, and 4 are scalene. The #5 triangle is a mirror image of the #4, the 6 is a mirror of the 3, the 7 is a mirror of the 2, and the 8 is a mirror of the 1.

The first goal of the project was to design an origami fold pattern which would be able to fold into the shape of the unit strip in each of the two states shown in Figure 20. To accomplish this, the design of the origami was divided into four parts, one for each of the unique triangles. Each origami part would need to be able to fold into the deformed and undeformed state of its respective triangle within the mechanism. The fold patterns on the edges of adjacent triangles need to be compatible.

In order to understand how an origami pattern is synthesized it is important to understand the rules and conditions of origami that must be met in order for a fold pattern to be capable of folding down to a flat sheet. The rules are as follows:

1. The fold pattern must be two-colorable. This means that if each section of the fold pattern (enclosed by the fold lines) was colored with two alternating colors, then there can be no two adjacent sections of the same color [76]. Another way of explaining this is that at every *node* (where fold lines meet) there must be an even number of fold lines that meet at the node.
2. Maekawa's theorem states that the sum of all positive (mountain = +1) and negative (valley = -1) fold lines entering a node must be a positive or negative even number [77] e.g. +2, -2, +4, -4, etc.
3. Kawasaki's theorem states that at every node, if the sections around the node were numbered, then the sum of the odd angles must be equal to 180°. The same must be true for the even sections [78].

www.manaraa.com

4. Self-intersections cannot occur at overlaps [79].

Another way of thinking about rules 1 and 2 is that the paper surrounding each node (fold line intersections) acts as parts of a spherical mechanism, where the fold lines are the joints and the sections between the folds are the links [81]. Rules 1 and 2 guarantee that each spherical mechanism has mobility.

3.2 Design

In designing our origami pattern we chose solutions with minimal Degrees Of Freedom (DOF's). We recognize that this type of problem could be solved in multiple ways, including designs similar to the Miura map pattern [82]. There has also been related research in this type of topological analysis [80]. We are assuming that our approach will result in fewer fold lines and hence will reduce cost and complexity of the final design. Our design process for the origami fold pattern is as follows:

1. Design of the footprint (the outer edges)
2. Adding fold lines that allow for the morphing of the outer edges
    a. First for the undeformed unit strip
    b. Then for the deformed unit strip
3. Adding fold lines to satisfy the origami design rules
    a. First for the undeformed unit strip
    b. Then for the deformed unit strip

المنارة للاستشارات
www.manaraa.com

3.2.1 Design of the Footprint (Outer Edges)

In order for a piece of origami to take on the undeformed and deformed state, a third state, the *printed* state was necessary. This means that the origami will be printed in one state (a non-regular hexagon), and it can then be folded into the undeformed and deformed states thereafter. Once the deformed and undeformed fold patterns were designed, they were superimposed onto one another to form the final fold pattern, which can fold to either the deformed or the undeformed state.

As shown in Figure 21 the sides of each triangle in their undeformed states are denoted as L_1, L_2, and L_3, where L_1 is the hypotenuse of the triangle, L_2 is the first side clockwise of the hypotenuse, and L_3 is the second side clockwise of the hypotenuse. The interior angles of each triangle are denoted as θ_1, θ_2, and θ_3, where θ_1 is opposite L_1, θ_2 is opposite L_2, and θ_3 is opposite L_3. In their deformed states, the sides are denoted as $\boldsymbol{\ell}_1$, $\boldsymbol{\ell}_2$, and $\boldsymbol{\ell}_3$, and the angles are denoted as θ_1', θ_2', and θ_3' where θ_1' is opposite $\boldsymbol{\ell}_1$, θ_2', is opposite $\boldsymbol{\ell}_2$, and θ_3', is opposite $\boldsymbol{\ell}_3$.

The angle bisectors in Figure 21A and B separate what will be referred to as the minor triangles, which are useful in defining the morphing from the printed state to the deformed and undeformed states.

(A) (B)

Figure 21 Labeling convention for the major triangles in the undeformed (A) and deformed (B) states. The example shown is applicable to triangle #2 in Figure 19.

Publication and ASME copyright pending presentation at the ASME IDETC2016 conference, August 21-24, 2016, Charlotte, NC

www.manaraa.com

As shown in Figure 22, the footprint is comprised of sides S_1, S_2, and S_3, where S_1 is the larger of L_1 and $\boldsymbol{\ell}_1$, S_2 is the larger of L_2 and $\boldsymbol{\ell}_2$, and S_3 is the larger of L_3 and $\boldsymbol{\ell}_3$. The angles of the footprint are θ_1', θ_2', and θ_3'. In designing the origami fold pattern, the sides of the footprint (S_1, S_2, and S_3) could be oriented parallel to the sides in Figure 21A, Figure 21B, or neither. The orientation of the sides in Figure 22 is parallel to the orientation of the sides in Figure 21B. This was done because it was found to be the simplest solution after trying all three methods. Throughout this Chapter, simplest means that it was simplest to synthesize and operate because the L-infinity norm of the number of folds between the deformed and undeformed states was smaller. Folding to the deformed state requires side length changes, while going to the undeformed state does not, therefore it was simpler to make the footprint parallel to the deformed state, thus reducing the complexity of the more complex state.

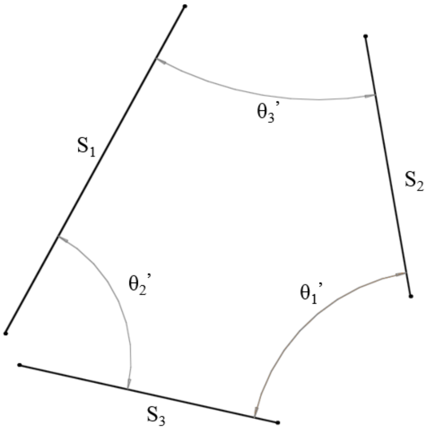

Figure 22 Nomenclature for the footprint (shown for the #2 triangle). The distance between the endpoints of the S's is arbitrary at this point

www.manaraa.com

3.2.2 Morphing the Outer Edges

Each major triangle is then sub-divided into three minor triangles, one for each of the sides of the major triangle. In this context the minor triangles each represent a rigid plane, and the space between the minor triangles represents the joints connecting the rigid planes.

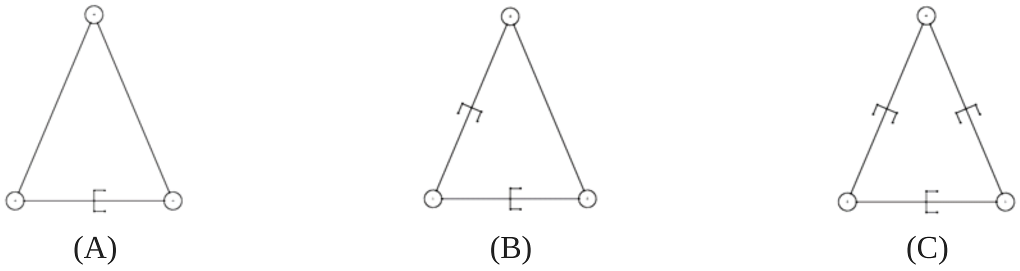

Figure 23 1 DOF triangle mechanism (A), 2 DOF triangle mechanism (B), and 3 DOF triangle mechanism (C)

As shown in Figure 23C, in the most generic case, the major triangles each have three sides and three angles, all of which can potentially change (the triangles in Figure 23 are kinematic models, their dimensions do not coincide with the dimensions of the triangles in the project). Each of the sides can change length and each of the corners can rotate to change its angle. If all three sides and all three angles change, the mechanism has three degrees of freedom. In the case of triangle 1 (from Figure 20), all three angles change and only one side length will change, making it a one DOF triangle, similar to the model shown in Figure 23A. In the case of triangles 2, 3, and 4 all three angles change, and two sides change length making them two DOF triangles, similar to the one shown in Figure 23B.

The number of DOF in each triangle is a design choice. Even if only one side is required to change length (as in triangle #1), it is still possible to initially extend the triangle’s side lengths and then later compress them during operation. For this problem, the triangles were chosen to be

www.manaraa.com

one and two DOF instead of three because they were found to be simpler to synthesize and operate, during experimentation. For the origami to go from the printed state to the undeformed state, all three angles must change, and all three sides must stay the same in length (for triangles #2 - #7). The angles that form the minor triangles are calculated as follows:

$$\varphi = \frac{1}{2}(\theta_3') \tag{25}$$

$$\psi = \frac{1}{2}(\theta_1') \tag{26}$$

$$\alpha = \frac{1}{2}(\theta_2') \tag{27}$$

where φ, ψ, and α are shown in Figure 24.

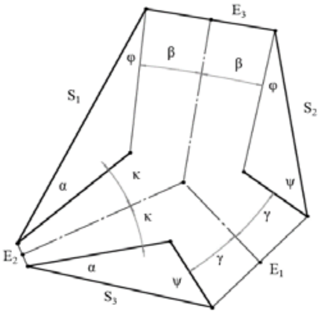

Figure 24 The footprint of the #2 triangle with the undeformed minor triangles shown

The minor triangles are the ones adjacent to sides S_1, S_2, and S_3 and are the same as the ones shown in Figure 21A. Connecting lines (E_1, E_2, and E_3) between the minor triangles have also been added for Figure 24. Although the geometry of the outer shape in Figure 24 forms a non-regular hexagon, when it is folded into the undeformed state, it forms the triangle shown in Figure 21A. The sides E_1, E_2, and E_3 are not sides of the triangle, they simply bridge the gaps between the minor triangles. The angles β, γ, and κ are the *excess* angles.

Publication and ASME copyright pending presentation at the ASME IDETC2016 conference, August 21-24, 2016, Charlotte, NC

www.manaraa.com

$$\beta = \frac{1}{2}(\theta_3' - \theta_3) \tag{28}$$

$$\gamma = \frac{1}{2}(\theta_1' - \theta_1) \tag{29}$$

$$\kappa = \frac{1}{2}(\theta_2' - \theta_2) \tag{30}$$

It is noteworthy that the signs of β and γ are negative while the sign of κ is positive. The result of this is that the lines defining the angle κ converge exterior to the hexagon while the lines defining the β and γ converge towards the interior of the hexagon.

This process is then repeated to form the minor triangles associated with the deformed triangle. In order to go from the printed state to the deformed state, the origami would need to close the gaps between the minor triangles and have two of the side lengths change. The angles that form the deformed minor triangles are calculated as follows:

$$\varphi' = \frac{1}{2}(\theta_3) \tag{31}$$

$$\psi' = \frac{1}{2}(\theta_1) \tag{32}$$

$$\alpha' = \frac{1}{2}(\theta_2) \tag{33}$$

المنارة للاستشارات

www.manaraa.com

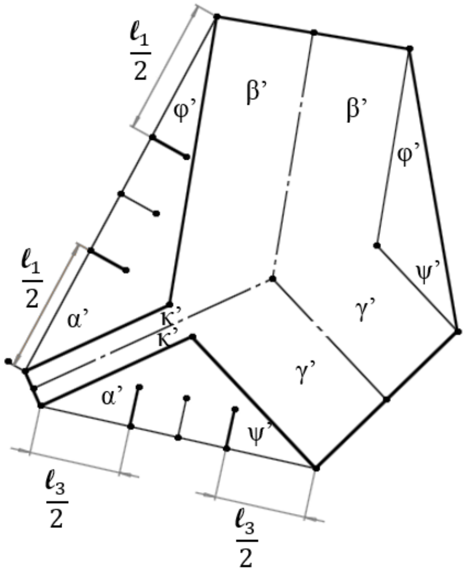

Figure 25 The footprint of the number 2 triangle with the deformed minor triangles is shown. The outer edges are the same as the ones in Figure 24.

The three lines perpendicular to the left and bottom sides of Figure 25 represent lines that allow shortening of those respective sides. A design choice that was made to simplify folding of the origami was that β', γ', and κ' are all zero. The reason this was done was because it was observed that in general, a fold that is pure translation (such as the gaps between the minor triangles in Figure 25) is easier to make than a fold that is both translation and rotation (such as the gaps between the minor triangles in Figure 24). The choice was that either β, γ, and κ could be zero, or β', γ', and κ' could be zero. The reason that the deformed major triangle was given the zero angles at the gaps between the minor triangles was because there are more complicated folds in this state, due to the length changes on the sides. The reason that the undeformed and deformed triangles could not both have zero degree excess angles was because if they did then their footprints would not be the same.

www.manaraa.com

The lines shown in Figure 24 and Figure 25 are sufficient to morph the outer edges of the printed state to the deformed and undeformed states respectively, but do not a represent a complete origami fold pattern due to the fact that they are missing lines in the interior.

3.2.3 Satisfying Origami Design Rules

It is noteworthy that there exists multiple solutions to the interior of each printed state. The solutions that were chosen for each of the printed states were the ones that were observed to be the simplest of the found solutions. The method for finding possible solutions to the interior of the printed states was based on observing the rules of origami and experimentation. The experimental part consisted of printing the triangle as seen in Figure 24, making the folds that were known to be necessary, then folding the remainder down flat. It was observed that when folding the remainder of the material down flat, a number of new nodes would be introduced to the fold pattern, and that the number of new nodes was dependent on the number of enclosed origami sections that were adjacent to the remainder material. Meaning, the more origami sections that were adjacent to the remainder material, the more new nodes would be introduced to the fold pattern. After this is done it can be readily observed where the necessary fold lines occurred in the interior of the printed state. The lines are then adjusted to ensure that the final dimensions are correct, as prescribed by the design of the mechanism. The final design for the undeformed version of triangle #2 is shown in Figure 26.

المنارة للاستشارات

www.manaraa.com

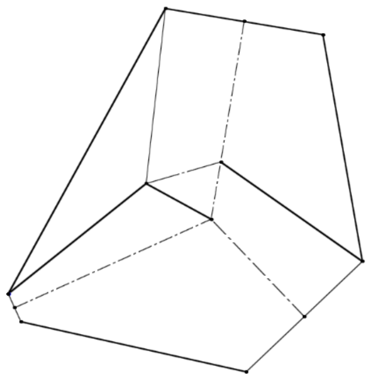

Figure 26 Final drawing for the origami for the undeformed triangle #2

The solid lines at the borders of the design are not fold lines. The solid lines within the drawing are positive folds. The centerlines are negative folds. The minor triangle that previously existed at the bottom of the hexagon was part of the design process but does not get folded and so was removed from the final design. These conventions are maintained throughout the remainder of the drawings.

The fold pattern for the undeformed triangle was simpler to synthesize, in part because it is a right triangle, and two of the angles are equal. The method for determining the interior fold lines for the printed state was to make the exterior folds for the deformed state, then to flatten the interior and observe the resulting fold lines. As can be seen in Figure 27 the deformed triangle was more complicated because of the length changes of the sides. The final drawing for the deformed triangle #2 is shown in Figure 27.

www.manaraa.com

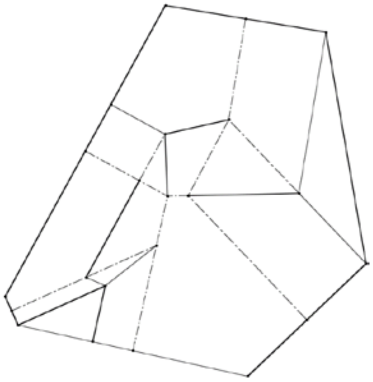

Figure 27 Final drawing for the origami for the deformed triangle #2

The process described in sections 2.2 and 2.3 is then repeated to generate fold patterns for the #3 and #4 triangles. The results are shown in Figure 28.

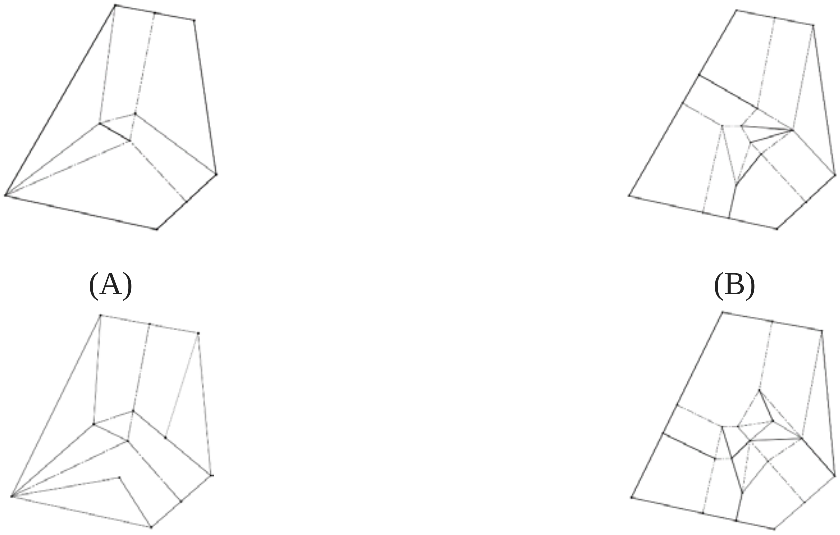

(A)

(B)

(C)

(D)

Figure 28 (A) Undeformed version of triangle #3, (B) deformed version of triangle #3, (C) undeformed version of triangle #4, and (D) deformed version of triangle #4

المنارة للاستشارات

www.manaraa.com

The process for synthesizing triangle #1 is slightly different from the other three. This is because only one of its side lengths changes, making this a simpler problem to solve. The procedure was similar for this triangle, however all of the length and angle changes were placed in the deformed state. The final drawing is shown in Figure 29.


(A) (B)

Figure 29 (A) Undeformed version of triangle #1 and (B) deformed version of triangle #1

All of the fold patterns shown up to this point are for the upper four major triangles of the unit strip (triangles 1-4 from Figure 20).

3.2.4 The Unit Strip

The geometry and kinematics of the lower four major triangles (#5-8 in Figure 20) of the unit strip are the same as that of the upper four (#1-4). The fold pattern however is slightly different for the deformed versions of the #3 and #4 triangle. The reason for this is because the fold lines along the adjacent edge of two major triangles must be the same. If the upper triangles were mirrored to form the lower triangles, they would have opposite direction Z-folds, which would not be continuous. In order to make the folds on adjacent edges continuous, the layering of the folds

المنارة للاستشارات
www.manaraa.com

must be opposite in the upper and lower triangles. The lower versions of these triangles are shown in Figure 30.


(A) (B)

Figure 30 The lower, deformed versions of the (A) #3 triangle and the (B) #4 triangle

As shown in Figure 31A, the undeformed versions of the major triangles are then assembled together to form the entire undeformed unit strip.

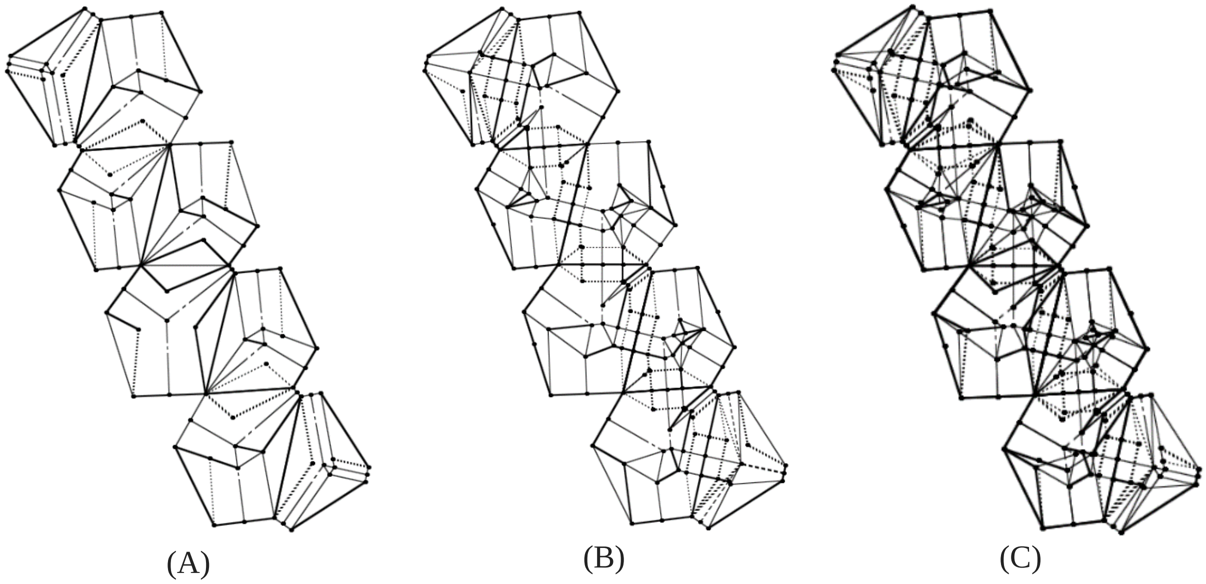
(A) (B) (C)

Figure 31 The complete fold pattern for the undeformed unit strip (A), the deformed unit strip (B), and the unified unit strip (C) (the undeformed and deformed superimposed onto one another)

المنارة للاستشارات

www.manaraa.com

As shown in Figure 31B, the deformed versions of the major triangles are then assembled together to form the complete deformed unit strip. The final fold pattern is created by superimposing the undeformed unit strip onto the deformed unit strip, this creates the final, unified unit strip, seen in Figure 31C.


(A) (B)

Figure 32 Undeformed (A) and deformed (B) mechanism, with unit strips of the origami mounted to it

The mechanism in each of its states, with one unit strip of the origami mounted to it is shown in Figure 32. Figure 32 shows two separate, static structures, where the undeformed origami is in blue and the deformed origami is in yellow.

3.3 Conclusion

In this project, a process has been demonstrated for synthesizing an origami fold pattern which can fold to two different versions of a triangle. This ability allows for a membrane with an origami fold pattern on it to mimic the kinematics of another shape-shifting mechanism. In this

المنارة للاستشارات
www.manaraa.com

way, such a membrane could be used as a waterproofing barrier for the mechanism that it mimics. Future plans for this project are to mount the unified origami (shown in Figure 31C) to Alqasimi's mechanism, which morphs from a cylinder to a hyperboloid. Future plans for this project are to make the folding of the origami automated and simpler, as well as measuring its efficacy as a waterproof barrier.

المنارة للاستشارات

www.manaraa.com

CHAPTER 4: STRESS-LIMITING TEST STRUCTURES FOR RAPID LOW-COST STRENGTH AND STIFFNESS ASSESSMENT

Portions of Chapter 4 were previously published to the Solid Freeform Fabrication conference in 2014 where it won an award for one of the best papers in conference and was automatically submitted to, and then published in the Rapid Prototyping Journal in 2015 and has been reproduced with permission from Emerald Group Publishing. I (Andrew Katz) was the first author, my advisor Dr. Craig Lusk, as well as Dr. Nathan Crane and Justin Nussbaum were also authors [83]. The specimen design and simulation sections of the paper were my primary contributions, however I did also help write other parts of the paper.

4.1 Introduction

Additive manufacturing (AM) refers to processes that build up parts by adding material under computer control. This enables the fabrication of a wide variety of different geometries with drastically reduced costs of variety [84]. However, the process does not just form geometry, it forms a material locally. In many processes, the material properties are sensitive to the processing methods and may vary with parameters such as position, orientation and ambient conditions to name a few [85] - [89]. As AM processes move from making interesting geometries, to producing functional parts and systems, the control of these properties becomes increasingly important [90].

This article is © Emerald Group Publishing and permission has been granted for this version to appear in the University of South Florida Repository. Emerald does not grant permission for this article to be further copied/distributed or hosted elsewhere without the express permission from Emerald Group Publishing Limited.

المنارة للاستشارات
www.manaraa.com

To address this challenge, there is an increasing focus on process monitoring and control, particularly online process monitoring [91], [92].

There is also a need for effective monitoring of the finished products. The objective of this work is to describe a low cost means of evaluating the modulus (resistance to deflection) and strength (resistance to failure) of thin beams printed using Additive Manufacturing (AM) processes. To this end, we describe two tests, the first of which, the stiffness test, is non-destructive, and the second, the strength test, when conclusive, results in fracture or permanent deformation of the part. Both tests require limited or no specialized measurement equipment and can be performed using a simple printed structure illustrated in Figure 33.

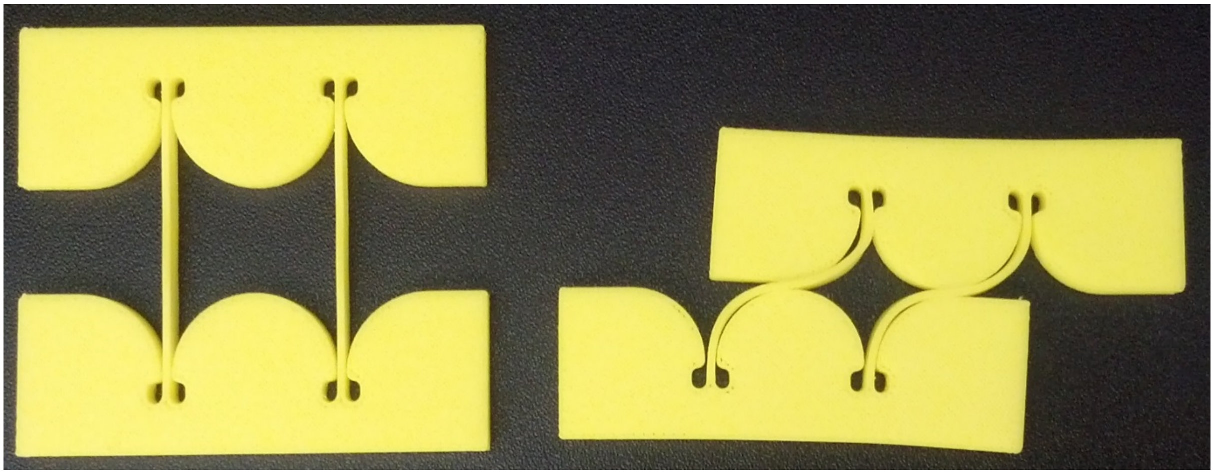

Figure 33 Photo of the basic test geometry in its “as-printed” (left) and deformed (right) positions

These tests are intended to complement and perhaps substitute for the standard tensile and flexural bending tests which are performed using immobile and expensive tensile testing equipment. They may also have some utility in process control or material evaluation, in that they

This article is © Emerald Group Publishing and permission has been granted for this version to appear in the University of South Florida Repository. Emerald does not grant permission for this article to be further copied/distributed or hosted elsewhere without the express permission from Emerald Group Publishing Limited.

www.manaraa.com

capture the key performance measures for structural integrity in simple, inexpensive tests. Thus, researchers seeking to improve the properties of an AM material could use these tests to ensure that they had not seriously compromised the structural utility of the material. The test method could be applied in production as an inexpensive method of verifying the stability of the production process. It may also provide a simple way for Do It Yourself (DIY) 3-D printing enthusiasts to assess the quality and stability of their processes using equipment they already have available.

The theory on which the measurement method is based is reviewed below. The subsequent sections describe how this design was implemented and tested using thermal extrusion processes. Stress test results are reported for a series of parts produced on a Stratasys Dimension 768 system. Stiffness measurements are reported for parts produced on two different thermal extrusion systems: RepStrap, and the Dimension 768. All tests were done using Acrylonitrile Butadiene Styrene (ABS) materials, each with its own feedstock.

4.2 Theory

We first describe the theoretical basis for the stiffness test. Our measurement method is based on measuring the natural frequency of a printed test structure. Vibrational frequencies of cantilever beams have previously been used to measure the modulus of elasticity of a variety of materials using both force and optical sensing methods [93] - [95]. This method has been covered in detail by ASTM standard E1876-01 [96]. This method requires only the test part, a striking mechanism such as a hammer and frequency sensing device, which could be a smart phone with an accelerometer or a microphone depending on the material and natural frequency of the part.

This article is © Emerald Group Publishing and permission has been granted for this version to appear in the University of South Florida Repository. Emerald does not grant permission for this article to be further copied/distributed or hosted elsewhere without the express permission from Emerald Group Publishing Limited.

المنارة للاستشارات
www.manaraa.com

In order for a vibration to occur, there must be a disturbance of some of the mass in a system from equilibrium. Further, that system must be capable of producing a restoring force that drives the mass back to its equilibrium position. The interaction of the restoring force and the mass's inertia produce oscillatory motion about the equilibrium position of the mass. In its simplest form, the location of the mass is described by a position coordinate, *x(t)*, as a function of time. The differential equation describing the moving mass, *m*, of the system is given by:

$$m\ddot{x} + F(x) = 0. \tag{34}$$

When the displacement of the mass is small, and the mass does not rotate, the restoring force, *F(x)*, can often be written as a linear function of the position. Thus, when the equilibrium position is taken as the origin for the *x*-coordinate, the governing equation is:

$$m\ddot{x} + kx = 0 \tag{35}$$

where k is a measure of the stiffness of the system. The solution to equation (2) is given by equations of the form:

$$x(t) = A\cos(\sqrt{k/m}\ t + \varphi) \tag{36}$$

where A, and φ are the amplitude and phase respectively, and their values depend on the details of the system's disturbance from equilibrium. On the other hand, the frequency of the oscillation of the system, $\sqrt{k/m}$, only depends on the system stiffness and moving mass. For our test, the moving mass is estimated as half of the total mass of the printed part, based on the symmetry between the fixed lower half and the moving upper half. Thus, by measuring the vibration frequency, ω, of the part when it is tapped lightly, we can use the part's moving mass, *m*, to determine its stiffness:

This article is © Emerald Group Publishing and permission has been granted for this version to appear in the University of South Florida Repository. Emerald does not grant permission for this article to be further copied/distributed or hosted elsewhere without the express permission from Emerald Group Publishing Limited.

www.manaraa.com

$$k = m\omega^2 \tag{37}$$

the stiffness value, k, is specific to a given geometry and material, and can be used to track the repeatability of an AM machine's building of a target geometry.

The governing equation (35) neglects energy losses from the system, and so equation (36) predicts that the vibrations will occur *ad infinitum* at the same magnitude. Of course this never happens, and the length of time that a part vibrates is indicative of the speed at which energy is lost from the system as heat or sound. The exclusion of such damping effects means that equation (37) tends to slightly over-predict the stiffness of a system. The amount of over-prediction depends on the internal damping in the material. For example, we were able to observe thirty periods of oscillation in an ABS part but only eight periods of oscillation in an acrylic part with the same geometry. Thus, we would assume that there is lower damping in the ABS, and the stiffness value obtained using equation (37) is closer to correct for the ABS part than for the acrylic one.

In the parts we were testing, the restoring force was provided by two identical thin flexures undergoing bending when the moving mass was plucked. Based on the dimensional considerations, we can surmise that the first bending mode with the lowest frequency is the fundamental vibration mode. Additionally we can conclude that based on the physics of the problem and the necessity for consistent units that the stiffness of the beam can be related to geometric and material parameters as follows:

$$k = aEI/l \tag{38}$$

where E is the tensile modulus, I is the second moment of area, and l is the length of the beam. The proportional constant, a, is a dimensionless number that is specific to the shape of the part.

This article is © Emerald Group Publishing and permission has been granted for this version to appear in the University of South Florida Repository. Emerald does not grant permission for this article to be further copied/distributed or hosted elsewhere without the express permission from Emerald Group Publishing Limited.

www.manaraa.com

Theoretical values for a have been tabulated for various ideal loading conditions [97], but these are difficult to relate effectively to actual parts because the proportional constant is quite sensitive to the specifics of how the beams are attached to the moving and fixed portions of the system. However, the constant, a, can be measured experimentally or predicted using Finite Element Analysis (FEA).

It may be desirable to compare the stiffness results of two parts which are printed from the same Computer-Aided Drawing (CAD) file using different process parameters or printing orientations. In this geometry, the stiffness will be particularly sensitive to the width of the flexible segments. Variations in other dimensions and the internal fill structure will be reflected in the overall weight of the part. The reference part could be a part of known properties or it could be the as-designed component using frequencies predicted analytically and calculated part mass. Taking the reference part as having mass, m_0, and stiffness, k_0, and the new part having mass, m_1, and stiffness k_1, we can define:

$$\alpha = m_1/m_0 \tag{39}$$

and

$$\beta = k_1/k_0. \tag{40}$$

From equation (37), the ratio of vibration frequencies of the two parts is:

$$\frac{\omega_1}{\omega_0} = \sqrt{\frac{\beta}{\alpha}}. \tag{41}$$

Using equation (38), taking the second moment of area for a rectangular beam, $I = w^3t/12$, and canceling the part thickness t, we can write equation (40) as:

This article is © Emerald Group Publishing and permission has been granted for this version to appear in the University of South Florida Repository. Emerald does not grant permission for this article to be further copied/distributed or hosted elsewhere without the express permission from Emerald Group Publishing Limited.

المنارة للاستشارات

www.manaraa.com

$$\beta = (E_1 w_1^3)/(E_0 w_0^3). \quad (42)$$

Then solving equations (39) – (42) for the ratio of moduli, we can see if process changes have affected the bulk stiffness of the material, by calculating:

$$E_1/E_0 = (m_1 \omega_1^2 w_0^3)/(m_0 \omega_0^2 w_1^3). \quad (43)$$

The second test measures the strength of the material used in a bending test. This test does not measure the strength directly but is based on the relationships between bending and internal moment, and internal moment and stress. The Bernoulli-Euler hypothesis asserts that the relationship between bending and the internal moment is:

$$M(s) = EI/R(s) \quad (44)$$

or in words, the moment at a point, $s\ \varepsilon(0,l)$, along a beam is equal to the beam stiffness, EI, divided by its radius of curvature (change in radius of curvature if initially curved). The stress due to bending is:

$$\sigma = My/I \quad (45)$$

where y is the distance from the neutral axis of the beam, which is a maximum at a distance $c = w/2$, i.e. half the width of the beam. Putting equations (11) and (12) together, and rearranging one finds that:

$$\sigma/E = c/R. \quad (46)$$

In other words, the ratio of stress to modulus equals the ratio of half the width of the beam to the radius of curvature of the beam. This means that if a beam is bent across a series of circular cams (different R values), the stress in the beam will increase as the radii of the circular cams decrease. There is a certain radius cam for which the beam will experience its fracture stress or a

This article is © Emerald Group Publishing and permission has been granted for this version to appear in the University of South Florida Repository. Emerald does not grant permission for this article to be further copied/distributed or hosted elsewhere without the express permission from Emerald Group Publishing Limited.

للاستشارات المنارة
www.manaraa.com

0.2% offset yield strength (i.e. the stress which causes 0.2% permanent strain in the beam). These failure stresses can therefore be associated with specific geometries or cam radii, which can be fabricated as the test geometry. If the beam can be bent ninety degrees around the cam without experiencing failure, the beam is stronger than expected. Thus, by building and testing parts with decreasing test radii, increasingly severe stress tests may be imposed on the material. As equation (41) associates a specific stress with a given cam radii (assuming that the modulus is known), the tests allow bounds on the fracture stress to be found.

The situation is more complicated for materials with beams that do not fracture when bent across cams of the smallest feasible size. For example, we found using ABS beams of one millimeter width that we saw increasing amounts of plastic deformation but that fracturing a thin beam required a 180° fold of minimal radius. When beams undergo plastic deformation but do not fracture, we observe that the stress in the beam is constant in the section that is in contact with the cam.

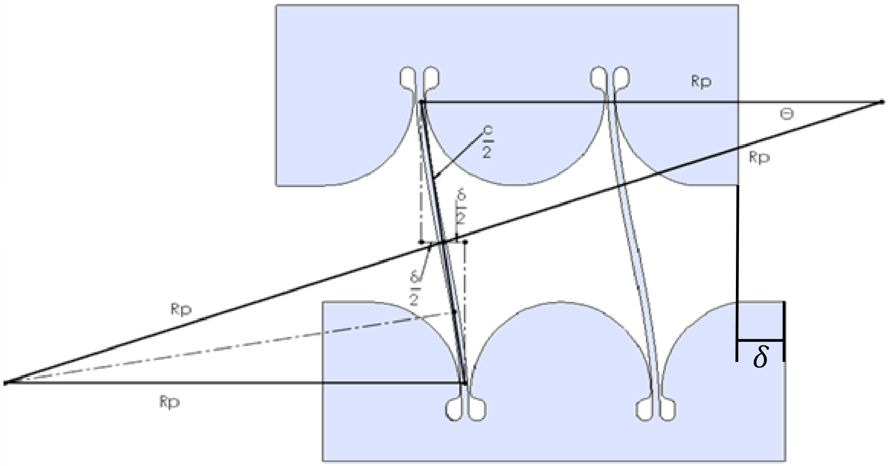

Figure 34 Geometry of the deformed test structure

This article is © Emerald Group Publishing and permission has been granted for this version to appear in the University of South Florida Repository. Emerald does not grant permission for this article to be further copied/distributed or hosted elsewhere without the express permission from Emerald Group Publishing Limited.

www.manaraa.com

We can therefore assume that the amount of residual plastic strain, ε_p, in the beam is constant along each half of the beam (one half of the beam is bent across the bottom cam and the other half is bent in the opposite direction across the top cam). Thus, each half of the beam is deformed into a circular arc, with radius R_p, subtended arc θ, and arc-length $L/2$. Using the geometry of circular arcs, we find:

$$R_p\theta = L/2 \tag{47}$$

and

$$R_p(1-\cos(\theta)) = \delta/2 \tag{48}$$

where δ is the horizontal translation of the top of the part relative to the bottom caused by the plastic deformation of the thin beams. This can be related to the residual plastic strain in the fibers of the beam by particularizing equation (46) as follows:

$$\varepsilon_p = \sigma/E = c/R_p. \tag{49}$$

By combining equations (47) - (49), we can express δ in terms of the residual strain, and the beam width and length as:

$$\delta = \frac{w}{\varepsilon_p}\left(1 - cos\left(\frac{L\varepsilon_p}{w_b}\right)\right). \tag{50}$$

Equation (50) can be used to solve for the residual strain, when the deformed horizontal translation is known. The displacement associated with a 0.2% strain is:

$$\delta = 500w\left(1 - cos\left(\frac{L}{500w}\right)\right). \tag{51}$$

On the other hand, we can compare the residual strain to the applied strain, which comes from bending the beams over the cams. The radius of curvature of the beams is:

This article is © Emerald Group Publishing and permission has been granted for this version to appear in the University of South Florida Repository. Emerald does not grant permission for this article to be further copied/distributed or hosted elsewhere without the express permission from Emerald Group Publishing Limited.

www.manaraa.com

$$R_d \; = \; R + c \tag{52}$$

where R_d is the radius of curvature of the beam, R is the radius of the cam, and c is half the width of the beam. The applied strain in the beam is:

$$\varepsilon_a = \sigma/E = c/R_d. \tag{53}$$

The strain recovered when the beam is unloaded is

$$\varepsilon_r = \varepsilon_a - \varepsilon_p. \tag{54}$$

4.3 Specimen Design

The test part is designed to leverage these pure bending effects possible with a cam to create a defined loading condition without requiring expensive testing equipment. Figure 35 defines the key parameters in the specimen design. The top and bottom rectangular sections provide both a solid base for attachment and a mass that drives the oscillation. Equation (46) was used to calculate what the radius should be. The beam width, $2c$, was selected based on the size of the feature we wished to test. These tests were done with a width of one millimeter. It should be noted that failure modes in AM parts can vary with size, but a smaller value of beam width ($2c$) will result in smaller test structures.

This article is © Emerald Group Publishing and permission has been granted for this version to appear in the University of South Florida Repository. Emerald does not grant permission for this article to be further copied/distributed or hosted elsewhere without the express permission from Emerald Group Publishing Limited.

www.manaraa.com

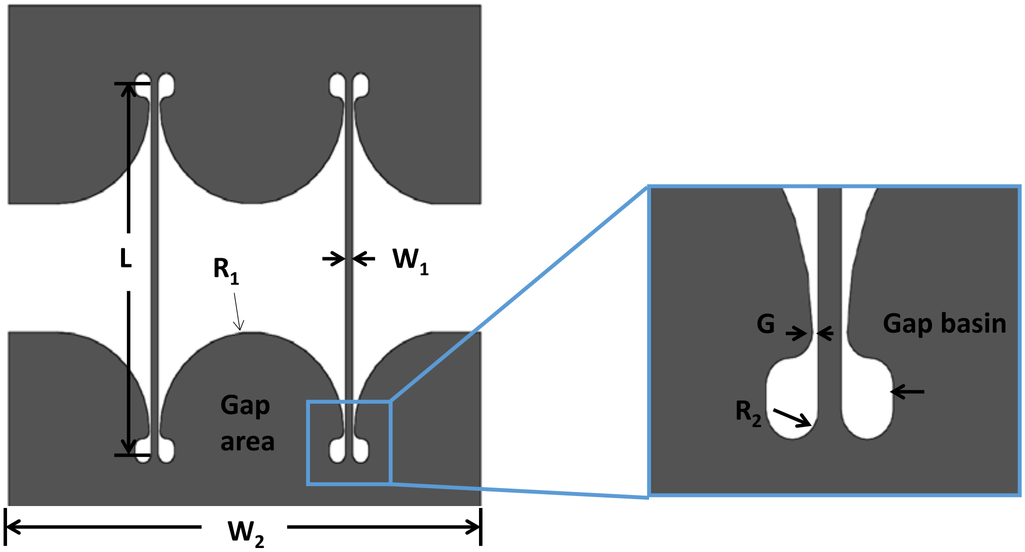

Figure 35 Definition of key geometric parameters in the test structure

This indicates what the cam radius should be to cause the beam to yield when bent across it. Using these basic relationships, a radius and beam width (c) can be selected that will evaluate the minimum strength of the specimen. The strength can be bracketed by testing a range of different specimen sizes.

Using a range of radii, one could find the smallest radius part would break or plastically deform and the largest radius part would not. More parts would be manufactured that were larger than the smallest radius until a radius value was found that does not break/deform the beam, but is only slightly larger than a radius which did break the beam. This would provide a lower bound for the ratio E/S_y. The same process would then be repeated starting from a large radius which did not cause failure in the beam, working down to a small enough radius that did cause failure in the beam, this process would confirm the ratio found in the previous step. Using a confirmed value of E, a value of S_y could then be determined, thus assessing the strength of the material. In process

This article is © Emerald Group Publishing and permission has been granted for this version to appear in the University of South Florida Repository. Emerald does not grant permission for this article to be further copied/distributed or hosted elsewhere without the express permission from Emerald Group Publishing Limited.

المنارة للاستشارات
www.manaraa.com

monitoring, it may be sufficient to print just a single size that confirms a minimum required strength.

The values for each of the cam radii used in this work can be found in Table 3 below. The other designs adjust the radius in steps of 10% of the nominal design D radius. The length of the beam was determined from equation (55)

$$L = \pi R + \varepsilon. \tag{55}$$

Table 3 Dimension values for each design of the part (in mm). All parts are 2.5 mm thick, except design I which is 5 mm.

Design	**Cam radius (R_1)**	**Beam length (L)**	**Beam width (W_1)**	**Gap (G)**	**Base fillet radius (R_2)**	**Part width (W_2)**	**Relative size**
A	8.98499	30.2272	1	0.25	1.13	66	0.7
B	10.2686	34.2596	1	0.25	1.13	66	0.8
C	11.5521	38.2921	1	0.25	1.13	66	0.9
D	12.8357	42.3246	1	0.25	1.13	66	1
E	14.1193	46.357	1	0.25	1.13	66	1.1
F	15.4028	50.3895	1	0.25	1.13	66	1.2
G	23.1043	74.5842	1	0.25	1.13	100	1.8
H	30.8057	98.7789	1	0.25	1.13	140	2.4
I	10.2686	34.2596	1	0.25	1.13	66	0.8

The beam must wrap around ninety degrees of the bottom cam and ninety degrees of the top cam. The factor of ε was two millimeters and was used to ensure that the beam was long enough to avoid a stress concentration at the base. The height of the parts was determined by the necessary length of the beam. In addition, it was necessary for there to be a space of material between the gap basin and the bottom/top edge of the part, this space was made to be at least seven millimeters in each of the designs. The gap basin was added because when there was no basin in the gap, the

This article is © Emerald Group Publishing and permission has been granted for this version to appear in the University of South Florida Repository. Emerald does not grant permission for this article to be further copied/distributed or hosted elsewhere without the express permission from Emerald Group Publishing Limited.

المنارة للاستشارات
www.manaraa.com

smallest that the gap could be made was limited by the feature size of the machine. By adding the basin, the nozzle of the machine could get a much smaller gap as shown in the figure depicting the gap. With this basin, the gap could be made as small as 0.25 mm, which is the value used in each of the designs. The radius of curvature of the deformed beam is described by equation (52). The walls of the gap basin were made curved so that there would be a smooth transition in the walls which would help to prevent additional stress concentrations. The beam width was one millimeter. Table 3 shows each of the dimensions for each size part. The relative size column refers to the size of the given design relative to the nominal size which is design D.

4.4 Test Procedures

Test components were fabricated from ABS filament on one of four thermal extrusion machines (Stratasys Dimension 768, Stratasys uPrint, Makerbot X2, and a custom-built RepStrap machine utilizing RepRap electronics). Replications of each part were produced with identical printing files to avoid any extra variations in the part. After printing, each part was weighed and the width of the flexible segments was measured using calipers. The weight and measured beam widths were used in the estimates of the strain and elastic modulus of the samples.

On the RepStrap components, the effective fill fraction was adjusted by changing the filament diameter setting in the control software to simulate the effect of variation in the filament diameter on the effective mechanical properties of the part. The parts were printed with settings of 2.9, 3.1, and 3.2 mm while the actual filament diameter varies between 2.9 and 3.0 mm. These variations in fill factor were changed to help us test how feed stock with slightly varying diameter can affect the mechanical properties of the printed parts.

This article is © Emerald Group Publishing and permission has been granted for this version to appear in the University of South Florida Repository. Emerald does not grant permission for this article to be further copied/distributed or hosted elsewhere without the express permission from Emerald Group Publishing Limited.

المنارة للاستشارات

www.manaraa.com

In addition to the test geometries described above, tensile and bending specimens were also prepared using the same printing parameters on both the Dimension and Custom-built RepStrap machines. Tensile and three point bend tests were conducted following ASTM standards D638-03 and D790-03 respectively.

A variety of methods exist for obtaining the vibrational response of a plucked part. For our tests, an inexpensive piezoelectric speaker was placed beneath the component, then clamped to a rigid structure (Figure 36). As the component vibrated the piezoelectric device output a voltage proportional to the force exerted by the oscillating free end. The piezoelectric speaker was then connected to an oscilloscope which provided the voltage vs. time response of the plucked part.

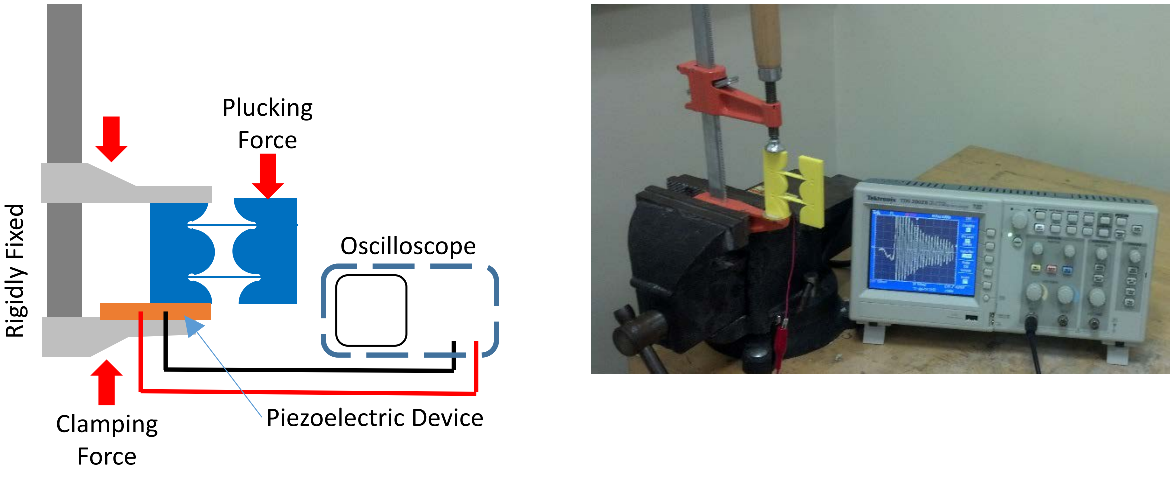

(A) (B)

Figure 36 Schematic diagram (A) of test setup (B) for measuring the vibrational frequency of a plucked part

If the component is metal and has a higher vibrational frequency, this test can be conducted with items as simple as a hammer and a microphone. A smart phone or tablet with an accelerometer

This article is © Emerald Group Publishing and permission has been granted for this version to appear in the University of South Florida Repository. Emerald does not grant permission for this article to be further copied/distributed or hosted elsewhere without the express permission from Emerald Group Publishing Limited.

www.manaraa.com

can also be used. By placing the part on the device and striking it, the accelerometer can pick up the vibrations.

The plastic strain of the samples was evaluated by deforming the beams around the cam surfaces and then removing the loads. These loads were applied by hand while the part lay horizontal on a flat surface. During deformation, the samples were visually monitored to verify that they remained in contact with the cam surface. The deformed position was maintained for less than five seconds before being released. The parts were gently vibrated to reduce the impact of friction on the final position of the component. The residual horizontal offset between the top and bottom of the structure was then measured to the nearest 0.5 mm as an indication of the relative plastic deformation of the structures. These tests were done on samples A-H which were produced on the Dimension machine. The residual offset distance and the measured beam widths were used to calculate the residual strain using equation (50). Results are based on one sample of each part size.

Vibration modulus testing was also conducted on the RepStrap specimens as well as on the Dimension 768 machine. These results were compared against tensile and three point flexural tests conducted on an 858 Material Testing System (MTS). The results for the Dimension 768 were also compared with the manufacturer’s specifications. The test specimen for the tensile and flexural tests produced by the RepStrap used layer heights of 0.5 millimeters thick and an infill angle of 45 degrees. The samples produced by the commercial Dimension 768 machine used layer heights of 0.25 millimeters. The infill angle formed by the Dimension 768 machine is unknown, however it can be assumed that it has been optimized to increase the strength of the part. Both the tensile and

This article is © Emerald Group Publishing and permission has been granted for this version to appear in the University of South Florida Repository. Emerald does not grant permission for this article to be further copied/distributed or hosted elsewhere without the express permission from Emerald Group Publishing Limited.

www.manaraa.com

flexural test specimens were 1 millimeter thick, the same thickness as the beam width for the test structure.

4.5 Simulation

Finite Element Analysis (FEA), modal analysis was performed on the design geometry to compare to the measured vibration frequencies. The simulation assumed ABS properties of E = 2.0 GPa and a density of 1.02 g/cm^3.

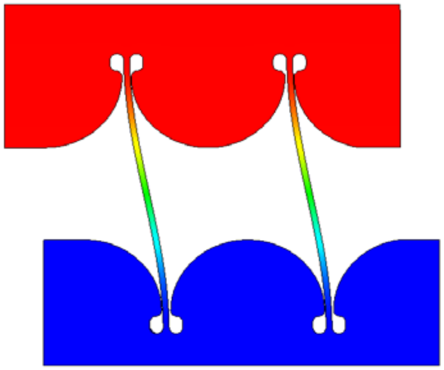

Figure 37 Mode one vibrations as shown in Solidworks FEA

The resulting mode shape is shown in Figure 37. As Table 4 shows, the difference between the measured frequencies and the simulated frequencies was relatively small for most of the parts. The exceptions are Parts G, H, and I. Parts G and H were the largest parts and the measured frequency appears to be the third mode. The FEA predicted third mode frequencies on parts G and H of 15.225 Hz. and 7.61 Hz. respectively. The difference between measured values and FEA predictions of the third mode is 15.42% and 4.58% respectively. The difference between measured values and FEA for part I was attributed to dimensional errors from manufacturing. When the

This article is © Emerald Group Publishing and permission has been granted for this version to appear in the University of South Florida Repository. Emerald does not grant permission for this article to be further copied/distributed or hosted elsewhere without the express permission from Emerald Group Publishing Limited.

www.manaraa.com

results were corrected for part mass and beam width, the modulus of elasticity estimation was consistent with other parts. Given the close match between the measured and simulated frequencies of the other parts, it is likely that the measured frequency for parts G and H were in fact the third vibrational mode.

Table 4 Frequency values for each part from vibrations tests and FEA in Hz

	Part A	**Part B**	**Part C**	**Part D**	**Part E**	**Part F**	**Part G**	**Part H**	**Part I**
Measured values	41.6	35.1	30.9	24.9	22.4	16.7	18.0	8.0	18.7
FEA	39.5	32.6	28.1	23.2	21.2	18.1	7. 2	3.8	33.0
Difference	5.1%	7.1%	8.9%	6.7%	5.4%	-8.3%	60%	52%	76.3%

Table 5 Specimen production scope

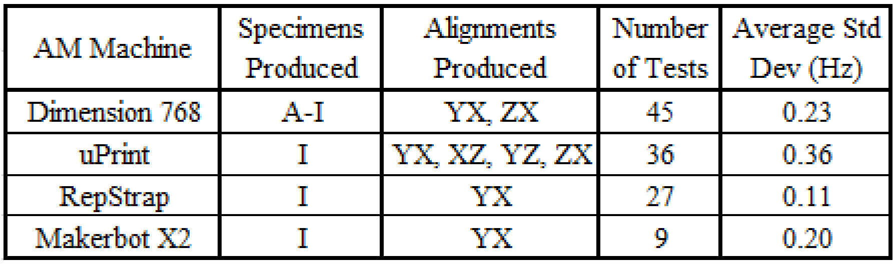

AM Machine	Specimens Produced	Alignments Produced	Number of Tests	Average Std Dev (Hz)
Dimension 768	A-I	YX, ZX	45	0.23
uPrint	I	YX, XZ, YZ, ZX	36	0.36
RepStrap	I	YX	27	0.11
Makerbot X2	I	YX	9	0.20

4.6 Results

The measured frequency data generally showed excellent repeatability for each individual part as seen in Table 5. The notable exceptions are parts G-1 and H-1. However, these samples appear to have been vibrating in multiple modes as discussed above.

The relationship of equation (43) was applied to the samples using the nominal (as-designed) density and FEA predictions of vibrational frequency to estimate the effective modulus

This article is © Emerald Group Publishing and permission has been granted for this version to appear in the University of South Florida Repository. Emerald does not grant permission for this article to be further copied/distributed or hosted elsewhere without the express permission from Emerald Group Publishing Limited.

المنارة للاستشارات
www.manaraa.com

of elasticity for each combination of geometry and machine tested. The resulting vibration frequency calculations are grouped by machine and printing parameters and summarized in Table 5 compared to the bending and tensile test data. The vibration data results were consistent with the values obtained by traditional tensile and bending methods. The standard deviations obtained from the RepStrap system were comparable in both cases. The high standard deviations in specimens G and H are attributed to measuring additional modes of vibration as also seen in Table 4. However, the parts produced on the commercial Dimension 768 machine produced more repeatable modulus measurements using the flexural and bending tests than was achieved with the vibration method.

In order to determine how the printing orientation effected the modulus, the Stratasys uPrint and Dimension 768 were used to print the test structure in various orientations. The natural frequency was then recorded and used to find the modulus of elasticity as summarized in Figure 39. There is a close resemblance with the manufacturer’s data for the specimens that were printed on-edge or flat on this print bed. The modulus values are expected to be similar as the deposition lines are oriented parallel with the print bed, unlike the upright orientation. However, the test specimens that were printed in the non-ideal orientation, standing up on the build platform in the Z-direction produced a significantly lower modulus as has been reported previously by Stratasys [98] and others [99].

By changing the effective filament diameter for the RepStrap in the control software to simulate a feed stock that was produced out of specification we are able to study effects on the mechanical properties. As the effective diameter of the filament was decreased, the AM machine increased the amount of material used, which produced a heavier part with a higher frequency and modulus. Since the natural frequency is related to the square root of the stiffness divided by the

This article is © Emerald Group Publishing and permission has been granted for this version to appear in the University of South Florida Repository. Emerald does not grant permission for this article to be further copied/distributed or hosted elsewhere without the express permission from Emerald Group Publishing Limited.

المنارة للاستشارات
www.manaraa.com

mass (equation (37)), this is an indicator that the stiffness of the part has increased as well. A small standard deviation indicates good repeatability in manufacturing and measurement.

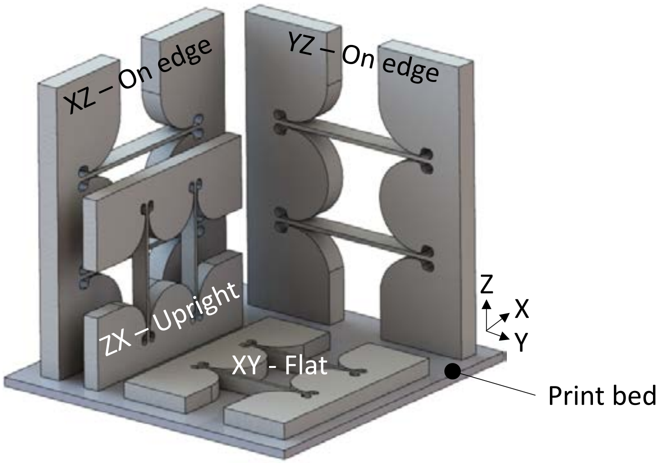

Figure 38 Printing orientations, parts not to scale

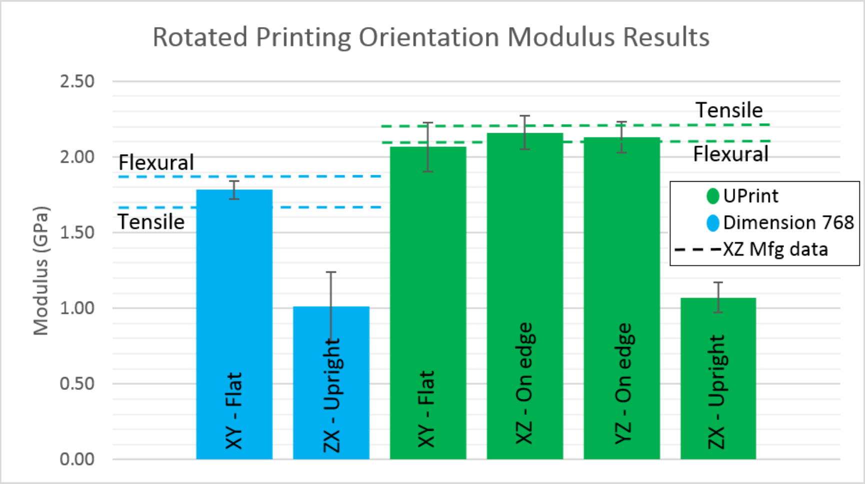

Figure 39 Modulus values measured by vibration method of test structures printed in various orientations

The measured vibrational modulus from the RepStrap was well below both the flexural and tensile modulus found from material testing system. However, they were closer to the results of

This article is © Emerald Group Publishing and permission has been granted for this version to appear in the University of South Florida Repository. Emerald does not grant permission for this article to be further copied/distributed or hosted elsewhere without the express permission from Emerald Group Publishing Limited.

المنارة للاستشارات
www.manaraa.com

the tensile tests than the flexural tests. This could be due to variations in the beam thickness throughout each part as well as other non-uniformities inherent in lower end 3D printers.

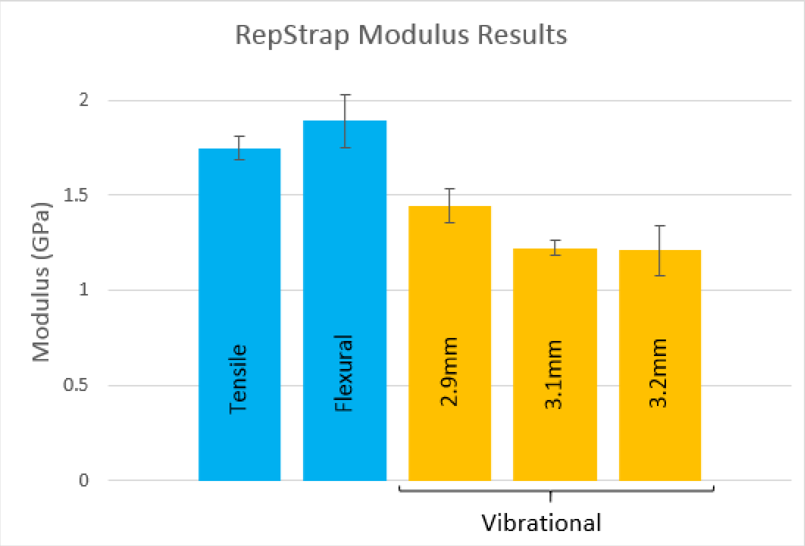

Figure 40 Mechanical properties from various tests. The vibrational tests were conducted with varied effective filament diameter.

The parts used in the strength test exhibited yielding but not fracture. Most of the tested parts had measurable deformations, i.e. the top portion of the part had translated a measurable amount from its original symmetric configuration as shown in Figure 33 (left) shows the deformations and calculated applied and residual strains for the tested parts. The results are consistent with the elastic behavior for specimens G and H, and a combination of elastic and plastic behavior for specimens A-F.

This article is © Emerald Group Publishing and permission has been granted for this version to appear in the University of South Florida Repository. Emerald does not grant permission for this article to be further copied/distributed or hosted elsewhere without the express permission from Emerald Group Publishing Limited.

www.manaraa.com

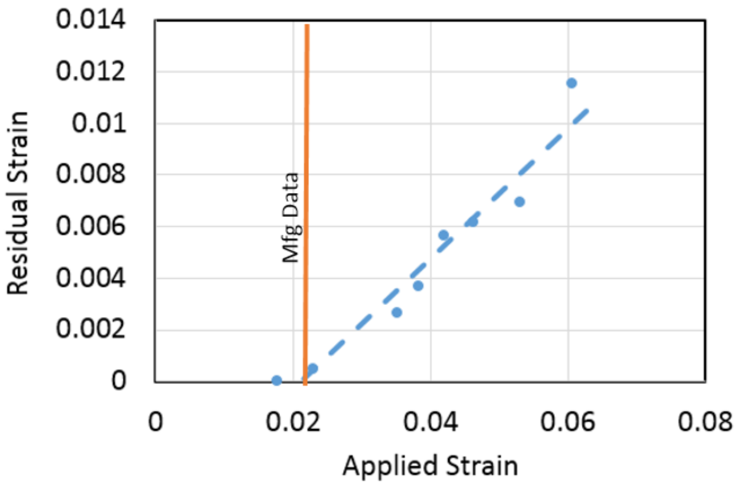

Figure 41 Residual plastic strain as a function of applied elastic strain. The x-intercept represents the onset of plastic strain.

The results are consistent with an elastic strain limit of approximately 2.1% as seen in Figure 41. This compares favorably to the elastic limit of 2.2% ($\varepsilon_{elastic\ limit} = S_y/E$) that would be estimated from the flexural data reported by Stratasys (S_{flex} = 41 MPa, E_{flex} = 1,834 MPa) [100].

4.7 Discussion

The modulus of bulk raw material is generally known, but the effective modulus of the printed structure can deviate significantly due to voids, under-filling, over-filling in the structure, anisotropy in the deposited material and other miscellaneous variations [87].

The yield strength (S_y) can also vary with the printing process due to the effects of temperature on the material and the bonding between features. There is also uncertainty in the actual value of *c* due to the tolerances of the manufacturing process. These differences will affect both the vibration frequency and the plastic deformation. Since these effects are not easily isolated,

This article is © Emerald Group Publishing and permission has been granted for this version to appear in the University of South Florida Repository. Emerald does not grant permission for this article to be further copied/distributed or hosted elsewhere without the express permission from Emerald Group Publishing Limited.

www.manaraa.com

it may be difficult to isolate the cause of a change. However, the measurements can be used to monitor for process changes that affect the density, finished dimensions, feature bonding, and material properties.

As each component is created by AM processes, the orientation or position of the part can vary the amount of void space or dimensional inaccuracies within a part. The vibrational analysis yields natural frequencies that vary little between tests of the same part but have a larger variation between individual parts with similar geometries. This would imply that the measuring system is repeatable, but each identical component produced from AM has varying degrees of inaccuracies. By simply measuring the weight of a component, a rough estimate of the degree of inaccuracies can be found. However this does not take into account how this would affect the mechanical properties of the component, namely elastic modulus. By using the equations found in the theory section we can then extract the estimated modulus values.

During the initial deformation of the test samples, audible pops were often observed for the small cam radii. Inspection of the specimens frequently showed delamination of the beams in these cases. Thus, these thin beams appear to be failing in shear rather than tension. This would be surprising for an isotropic material as the shear stress should be small under the expected load condition. This may indicate that the loading does not fully reach the idealized full bending condition. However, there is a concentration of shear as the beam transitions between the curvatures of the two cams. Additionally, the bonding between adjacent deposition lines is known to be weaker than the native polymer. This is especially possible in thin beams made without fill in which the software that defines the AM machine's route may be prioritizing accuracy of external dimensions over mechanical strength.

This article is © Emerald Group Publishing and permission has been granted for this version to appear in the University of South Florida Repository. Emerald does not grant permission for this article to be further copied/distributed or hosted elsewhere without the express permission from Emerald Group Publishing Limited.

www.manaraa.com

While the vibrations were measured using an oscilloscope in this work, the speaker output could be read by more commonly available computer inputs such as a microphone jack on a cellular phone or laptop. We have also demonstrated that we can detect the vibrations using the accelerometers built into many tablets and smart phones. Thus, these methods could be adapted to the use by DIY testers with minimal expense. They could also be integrated as test coupons in production manufacturing without the need to use expensive testing machines for routine process monitoring. However, to be useful in process monitoring, the test method needs to be highly reliable. While these results were promising, more evaluation is necessary to assess whether the method is sufficiently accurate to use in these applications. While the variation in the measurements was significant in the initial tests, it is unclear whether this is due to variation in the test methods or the parts being tested.

4.8 Conclusion

A simple test geometry has been presented that facilitates assessments of strain limits of the material and the elastic modulus. This method utilizes flexible elements and a circular cam to apply a uniform strain across the flexible elements utilizing simple hand loading. A series of different sized elements can be used to identify the elastic strain limit of the printed structures. Additionally, the natural frequency of the structure provides an estimate of the structure's elastic modulus. The required equipment is readily available to DIY users. The method could also be useful for monitoring the stability of production processes.

A series of components have been manufactured using thermal extrusion and the test methods were applied to them. When applied to a series of parts with different bend radii, the

This article is © Emerald Group Publishing and permission has been granted for this version to appear in the University of South Florida Repository. Emerald does not grant permission for this article to be further copied/distributed or hosted elsewhere without the express permission from Emerald Group Publishing Limited.

المنارة للاستشارات

www.manaraa.com

measured results provided an estimate of the elastic strain limit of the material. The elastic modulus estimates showed consistent predictions for components produced on the same machine even when the key geometric parameter (cam radius) varied. The method also showed an ability to detect the effects of a printing parameter on the effective modulus of elasticity of the printed structure. These results show that the outcomes, particularly the frequency, are sensitive to variations between parts. Further work is needed to identify the sensitivity of these measurements to other sources of process variation.

This article is © Emerald Group Publishing and permission has been granted for this version to appear in the University of South Florida Repository. Emerald does not grant permission for this article to be further copied/distributed or hosted elsewhere without the express permission from Emerald Group Publishing Limited.

المنارة للاستشارات
www.manaraa.com

CHAPTER 5: CONCLUSION

The overarching themes of my research have been compliant mechanisms and origami engineering. Two of the projects that comprise my dissertation (Chapters 2 and 3) involve using novel pieces of origami to make previously designed mechanisms waterproof. By creating pieces of origami whose kinematics mimic that of the underlying mechanism, the origami can be used as a waterproof membrane to prevent fluid flow through the mechanism during actuation of the mechanism. An example of how this could be used in application is that the second mechanism for which this concept was applied (the cylinder which deforms to a hyperboloid), could be used as a pipe. Given the shape-changing abilities of the mechanism, the pipe would be able to change cross section, which could be beneficial for curtailing or increasing fluid flow into an engine or pump. I created the origami membranes that they sought to create. I created an origami fold pattern which can fold into any of the positions that the shape-shifting surface is able to take on. This project also resulted in designs which reduced the internal stresses of the part during operation by more than 22%. In the second project [3], I created an origami fold pattern which can fold to either of the states that the SMSF can take on. In this work, I designed a membrane which could reduce the side length of the underlying mechanism by more than 30%.

In the third project [83] that was included in my dissertation, I developed a method for testing rapid prototyped materials after they have been processed through a rapid prototyper. When a material is processed through an FDM machine, it undergoes a thermodynamic process and a physical change in the structure of the material. These two events can cause a change in material properties. For this reason it is necessary to test the material properties after processing in order to

www.manaraa.com

know how the material is going to behave in operation. The part developed in this project allows the material to be tested after processing without the need for expensive testing equipment such as a tensile tester.

My contributions in Chapter 2 are:

- A novel design for an origami membrane whose kinematics when folded, mimic that of the shape-shifting surface [66].
- The optimization for the shape-shifting surface.

My contributions in Chapter 3 are:

- A method for synthesizing a novel origami fold pattern whose kinematics mimic that of another mechanism.
- The fold pattern for the origami to mimic the kinematics of the shape-morphing space frame.

My contributions in Chapter 4 are:

- The design of the test part and its FEA simulations.

Future work for Chapters 2 and 3 would involve developing methods for sensing and actuation of the parts with the origami mounted to it, as well as developing an integrated prototype that would consist of the mechanism and the origami being fabricated as one. It would also include developing methods for automating the folding of the origami, as well as exploring the possible advantages of simplifying the mechanisms themselves (i.e. reducing the number of components). Future work also includes, identifying the optimal material to be used for the origami membrane. For Chapter 4, future work could include further studying residual strain and the fatigue implications thereof, as well as seeking to develop a method for identifying the elastic modulus of the material with a cheaper means than an osciliscope.

www.manaraa.com

REFERENCES

[1] Howell, L. L., *Compliant Mechanisms*, Wiley, New York, 2001.

[2] Katz, A., Lusk, C., “Design and Kinematic Optimization of a Waterproof Shape-Shifting Surface (SSS)” in Proceedings of the ASME 2015 International Design Engineering Technical Conference & Computers and Information in Engineering Conference, Boston, MA, Aug. 2-5, 2015. DETC2015-47595, (2015).

[3] Katz, A., Lusk, C., “Design of an Origami Fold Pattern for Shape-Morphing Using Triangles” in Proceedings of the ASME 2016 International Design Engineering Technical Conference & Computers and Information in Engineering Conference, Charlotte, NC, Aug. 21-24, 2016. DETC2016-59604, (2016).

[4] Evans, A. A., Silverberg, J. L., Santangelo, C. D., “Lattice mechanics of origami tessellations” Physical Review E. 92, DOI: 10.1103/PhysRevE.92.013205, (2015).

[5] Terashima, T., Shimanuki, H., Kato, J., Watanabe, T., “Method for Representing 3-D Virtual Origami” in Proceedings of the 2005 Eight International Conference on Document Analysis and Recognition, 1520-5263/05, (2005).

[6] Hull, T., “On the Mathematics of Flat Origamis”, Congressus Numerantium, Vol. 100, pp. 215-224, (1994).

[7] Lang, R. J., “Mathematical Methods in Origami Design”, Bridges 2009: Mathematics, Music, Art, Architecture, Culture, (2009).

[8] Hagiwara, I., “Current Trends and Issues of Origami Engineering”, ICSC, Part I, CCIS 326, pp. 259-268, (2012).

[9] Lang, R. J., Demaine, E. D., “Facet Ordering and Crease Assignment in Uniaxial Bases”, in Proceedings of the 4th International Meeting of Origami Science, Math, and Education, Pasadena, California, September 8-10, pp. 189-205, (2006).

[10] Kishi, N., Fujii, Y., “Origami, Folding Paper Over the Web”, in Proceedings of the 3rd Asia Pacific Computer Human Interaction, July 15-17 (1998), pp. 337-342.

[11] Demaine, E. D., Demaine, M. L., “Recent Results in Computational Origami”, in Proceedings of the 3rd International Meeting of Origami Science, Math, and Education, Monterey, California, March 9-11, (2001), pp. 3-16.

www.manaraa.com

[12] Yellowhorse, A., Howell, L. L., “Creating Rigid Foldability to Enable Mobility of Origami Inspired Mechanisms”, Journal of Mechanisms and Robotics, Vol. 8/011011, DOI: 10.1115/1.4029923, February, (2016).

[13] Zhou, L., Marras, A. E., Su, H. J., Castro, C. E., “DNA Origami Compliant Nanostructures with Tunable Mechanical Properties”, American Chemical Society NANO, DOI: 10.1021/nn405408g, Vol. 8, No. 1, pp. 27-34, (2014).

[14] Yoo, J., Aksimentiev, A., “In situ structure and dynamics of DNA origami determined through molecular dynamics simulations”, PNAS, Vol. 110, No. 50, DOI: 10.1073/pnas.1316521110, (2013).

[15] Lang, R. J., “A Computational Algorithm for Origami Design”, in Proceedings of the Twelfth Annual Symposium on Computational Geometry, May 24-26, Philadelphia, PA, (1996).

[16] Ghourabi, F., Ida, T., Takahashi, H., Marin, M., Kasem, A., “Logical and Algebraic View of Huzita’s Origami Axioms with Applications to Computational Origami”, SAC, March 11-15, Seoul, Korea, (2007).

[17] Ghourabi, F., Ida, T., Kasem, A., “Proof Documents for Automated Origami Theorem Proving”, ADG 2010, LNAI 6877, pp. 78-97, (2011).

[18] Ida, T., “Huzita’s basic origami fold in geometric algebra”, in 16th International Symposium on Symbolic and Numeric Algorithms for Scientific Computing, DOI: 10.1109/SYNASC.2014.9, (2014).

[19] Ahmed, S., Ounaies, Z., Frecker, M., “Investigating the performance and properties of dielectric elastomer actuators as a potential means to actuate origami structures”, Smart Materials and Structures, 23, DOI: 10.1088/0964-1726/23/9/094003, (2014).

[20] Fuchi, K., Buskhol, P. R., Bazzan, G., Durstock, M. F., Reich, G. W., Vaia, R. A., Joo, J. J., “Origami Actuator Design and Networking Through Crease Topology Optimization”, Journal of Mechanical Design, Vol. 137/091401, DOI: 10.1115/1.4030876, September, (2015).

[21] Kim, D., Gillespie, R. B., “Origami Structured Compliant Actuator (OSCA)”, in 2015 IEEE International Conference on Rehabilitation Robotics (ICORR), pp. 259-264, (2015).

[22] Salerno, M., Zhang, K., Menciassi, A., Dai, J. S., “A Novel 4-DOF Origami Grasper With an SMA-Actuation System for Minimally Invasive Surgery”, IEEE Transactions on Robotics, (2016).

[23] McGough, K., Ahmed, S., Frecker, M., Ounaies, Z., “Finite element analysis and validation of dielectric elastomer actuators used for active origami”, Smart Materials and Structures 23, DOI: 10.1088/0964-1726/23/9/094002, (2014).

المنارة للاستشارات

www.manaraa.com

[24] Kuzuya, A., Yamazaki, T., Yasuda, K., Sakai, Y., Yamanaka, Y., Xu, Y, Aiba, Y., Ohya, Y., Komiyama, M., “Nanomechanical DNA Origami Devices as Versatile Molecular Sensors”, NEMS 2012, Kyoto, Japan, pp. 318-321, March 5-8, (2012).

[25] Delimont, I. L., Magleby, S. P., Howell, L. L., “A Family of Dual-Segment Compliant Joints Suitable for Use as Surrogate Folds”, Journal of Mechanical Design, Vol. 137/092302, DOI: 10.1115/1.4030875, September, (2015).

[26] Delimont, I. L., Magleby, S. P., Howell, L. L., “Evaluating Compliant Hinge Geometries for Origami Inspired Mechanisms”, Journal of Mechanisms and Robotics, Vol. 7/011009, DOI: 10.1115/1.4029325, February, (2015).

[27] Tolman, S. S., Delimont, I. L., Howell, L. L., Fullwood, D. T., “Material selection for elastic energy absorption in origami inspired compliant corrugations”, Smart Materials and Structures 23, DOI: 10.1088/0964-1726/23/9/094010, (2014).

[28] Yang, Y., Xia, Z., Zhao, X., Tokura, S., Hagiwara, I., “Comprehensive Optimization for Raised Floor Structure Using Origami Engineering”, ICSC 2012, Part I, CCIS 326, pp. 216-227, (2012).

[29] Thrall, A. P., Quaglia, C. P., “Accordion shelters: A historical review of origami-like deployable shelters developed by the US military”, Engineering Structures 59 pp. 686-692, (2014).

[30] Song, Z., Ma, T., Tang, R., Cheng, Q., Wang, X., Krishnaraju, D., Panat, R., Chan C. K., Yu, H., Jiang, H., “Origami lithium-ion batteries”, Nature Communications, DOI: 10.1038/ncomms4140, (2014).

[31] Zhao, X., Hu, Y., Hagiiwara, I., “Shape Optimization to Improve Energy Absorption Ability of Cylindrical Thin-walled Origami Structure”, Journal of Computational Science and Technology, Vol. 5, No. 3, DOI: 10.1299/jcst.5.148, (2011).

[32] Zhao, X., Hu, Y., Hagiwara, I., “Study on Crash Characteristics of Half Cut Type Vehicle Side Member Structure of Energy Absorption Ability by Using Origami Engineering”, Journal of Computational Science and Technology, Vol. 5, No. 1, DOI: 10.1299/jcst.5.13, (2011).

[33] Peraza-Hernandez, E. A., Hartl, D., Malak Jr., R. J., Lagoudas, D. C., “Origami-inspired active structures: a synthesis and review”, Smart Materials and Structures, 23, DOI: 10.1088/0964-1726/23/9/094001, (2014).

[34] Zhang, K., Qiu, C., Dai, J. S., “An Extensible Continuum Robot With Integrated Origami Parallel Modules”, Journal of Mechanisms and Robotics, Vol. 8/031010, DOI: 10.1115/1.4031808, June, (2016).

المنارة للاستشارات

www.manaraa.com

[35] Dzhavakhyan, R. P., Makhsudyan, N. A., Arakelyan, V. G., “Comparative Analysis and Synthesis of Plane Spherical Four-Hinge Mechanisms”, Journal of Machinery Manufacture and Reliability, ISSN 1052-6188, Vol. 40, No. 5, pp. 423-429, (2011).

[36] Shai, O., Müller, A., “Computational Algorithm for Determining the Generic Mobility of Floating Planar Spherical Linkages”, Computational Kinematics, Mechanisms and Machine Science 15, DOI: 10-1007/978-94-007-7214-4_22, pp. 193-200, (2014).

[37] Loch, A., Hollick, M., “Face the Enemy: Attack Detection for Planta Graph Routing”, Conference on Networked Systems, 978-0-7695-4950-7/12, DOI: 10.1109/NetSys.2013.16, (2013).

[38] Shai, O., Pennock, G. R., “Extension of Graph Theory to the Duality Between Static Systems and Mechanisms”, Journal of Mechanical Design, Vol. 128, pp. 179-191, January (2006).

[39] Kalinina, E. A., Khitrov, G. M., Pogozhev, S. V., “Linear Algebra Methods in Graph Theory”, Stability and Control Processes in Memory of V.I. Zubov (SCP), 2015 International Conference, DOI: 10.1109/SCP.2015.7342228, pp. 570-572, St. Petersburg, October 5-9, (2015).

[40] Yi, L., Leinonen, T., “Solution of Topology Embryonic Graph and Topology Graph for Unified Planar-Spatial Mechanisms”, in Proceedings of DETC’03 ASME 2003 Design Engineering Technical Conferences and Computers and Information in Engineering Conference, Chicago, Illinois, USA, September 2-6, DETC2003/DFM-48167, (2003).

[41] Zhongzhi, Y., “Some Inferences from Graph Theory of Eigenvalue Problem”, Kexue Tongbao, Vol. 26, No. 9, September, pp. 810-814, (1981).

[42] Simpson, J. O., Wise, S. A., Bryant, R. G., Cano, R. J., Gates, T. S., Hinkley, J. A., Rogowski, R. S., Whitley, K. S., “Innovative Materials for Aircraft Morphing”, in Proceedings of SPIE, the International Society for Optical Engineering, Vol. 3326, pp. 240-249, (1998).

[43] Wu, J., Li, J., Yan, S., “Design of deployable bistable structures for morphing skin and its structural optimization”, Engineering Optimization, DOI: 10.1080/0305215X.2013.800055, (2013).

[44] Thill, C., Etches, J., Bond, I., Potter, K., Weaver, P., “Morphing Skins”, Aeronautical Journal, ISSN: 0001-9240, Vol. 112, Iss. 1129, pp. 117-139, (2008).

[45] Funke, L., Schmiedeler, J. P., Zhao, K., “Design of Planar Multi-Degree-of-Freedom Morphing Mechanisms”, in Proceedings of the ASME 2014 International Design Engineering Technical Conferences & Computers and Information in Engineering Conference, August 17-20, Buffalo, New York, DETC2014-35265, (2014).

المنارة للاستشارات
www.manaraa.com

[46] Inoyama, D., Sanders, B. P., Joo, J. J., "Topology Synthesis of Distributed Actuation Systems for Morphing Wing Structures", Journal of Aircraft, Vol. 44, No. 4, DOI: 10.2514/1.25535, July-August, (2007).

[47] Inoyama, D., Sanders, B. P., Joo, J. J., "Topology Optimization Approach for the Determination of the Multiple-Configuration Morphing Wing Structure", Journal of Aircraft, Vol. 45, No. 6, DOI: 10.2514/1.29988, November-December, (2008).

[48] Li, Z., Bian, H., Shi, L., Niu, X., "Reliability-based Topology Optimization of Compliant Mechanisms with Geometrically Nonlinearity", Applied Mechanics and Materials, Vol. 556-562, DOI: 10.4028/www.scientific.net/AMM.556-562.4422, pp. 4422-4434, (2014).

[49] Sullivan, T., Van de Ven, J. D., "Topological Synthesis and Integrated Kinematic-Structural Dimensional Optimization of a Ten-Bar Linkage for a Hydraulic Rescue Spreader", in Proceedings of the ASME 2013 International Design Engineering Technical Conferences and Computers Information in Engineering Conference, August 4-7, Portland, Oregon, DETC2013-12327, (2013).

[50] Demko, J. A., Morrison, G. L., Rhode, D. L., "Effect of Shaft Rotation on the Incompressible Flow in a Labyrinth Seal", Journal of Propulsion and Power, Vol. 6, Iss. 2, pp. 171-176, (1990).

[51] Kushnir, A. P., "Passage of Pollutants through Contactless Seals with a Motionless Spindle", ISSN 1068-798X, Russian Engineering Research, Vol. 31, No. 1, pp. 53-55, (2011).

[52] Kushnir, A. P., Lizogub, V. A., "Contaminant Transmission through Contactless of Machine-Tool Spindles", ISSN 1068-798X, Russian Engineering Research, Vol. 32, No. 4, pp. 395-398, (2012).

[53] Li, J., Qiu, B., Feng, Z., "Experimental and Numerical Investigations on the Leakage Flow Characteristics of the Labyrinth Brush Seal", Journal of Engineering for Gas Turbines and Power, Vol. 134/102509, October, (2012).

[54] Brownell, J. B., Millward, J. A., Parker, R. J., "Nonintrusive Investigations Into Life-Size Labyrinth Seal Flow Fields", Journal of Engineering for Gas Turbines and Power, Vol. 111, Iss. 2, pp. 335-342, (1989).

[55] Rhode, D. L., Guidry, M. J., "Sharper Labyrinth Seal Edges to Allow Greater Clearance Without Increased Leakage", in Proceedings of the Computers in Engineering Conference and the Engineering Database Symposium, pp. 407-414, (1995).

[56] Deo, H., Zheng, X., "Flexure Design for Progressive Clearance Labyrinth Seal", in Proceedings of the ASME 2012 International Design Engineering Technical Conferences & Computers and Information in Engineering Conference, August 12-15, Chicago, IL, DETC2012-71535, (2012).

www.manaraa.com

[57] Silva, R. R., Lopes, J. G., Correia, J. R., “The effect of wind suction on flat roofs: An experimental and analytical study of mechanically fastened waterproofing systems”, Construction and Building Materials 24, DOI: 10.1016/j.conbuildmat.2009.08.034, pp. 105-112, (2010).

[58] Liljebäck, P., Stavdahl, Ø., Pettersen, K. Y., Gravdahl, J. T., “A Modular and Waterproof Snake Robot Joint Mechanism with a Novel Force/Torque Sensor”, in 2012 IEEE/RSJ International Conference on Intelligent Robots and Systems, October 7-12, Vilamoura, Algarve, Portugal, (2012).

[59] Sharma, D., Deb, K., Kishore, N. N., “Customized evolutionary optimization procedure for generating minimum weight compliant mechanisms”, Engineering Optimization, Vol. 46, No. 1, DOI: 10.1080/0305215X.2012.743535, pp. 39-60, (2014)

[60] Ohsaki, M., Tsuda, S., Watanabe, H., “Optimization of retractable structures utilizing bistable compliant mechanism”, Engineering Structures 56, pp. 910-918, (2013).

[61] Kang, K., Kim, K., Lee, H., “Evaluation of elastic modulus of cantilever beam by TA-ESPI”, Optics & Laser Technology 39, DOI: 10.1016/j.optlastec.2006.01.003, pp. 449-452, (2007).

[62] Munguía,J., Dalgarno, K. W., Reid, R., “Fatigue behavior of additive manufacturing parts. A preliminary analysis”, Innovative Developments in Virtual and Physical Prototyping: Proceedings of the 5th International Conference on Advanced Research and Rapid Prototyping, ISBN 978-0-415-68418-7, (2012).

[63] Wang, W., Yu, Y., “Analysis of frequency characteristics of compliant mechanisms”, Front. Mech. Eng. China 2007, 2(3): pp. 267-271, DOI: 10.1007/s11465-007-0046-2, (2007).

[64] Martina, F., Williams, S. W., Colegrove, P., “Improved Microstructure and Increased Mechanical Properties of Additive Manufacture Produced TI-6AL-4V by Interpass Cold Rolling”, in 24th International Solid Freeform Fabrication Symposium, Austin, Texas, pp. 490-496, (2016).

[65] Wittwer, J. W., Howell, L. L., “Mitigating the Effects of Local Flexibility at the Built-In Ends of Cantilever Beams”, Journal of Applied Mechanics, Vol. 71, DOI: 10.1115/1.1782913, pp. 748-751, (2004).

[66] Montalbano, P., Lusk, C., 2011, “Design Concepts for Shape-Shifting Surfaces” in Proceedings of the ASME 2011 International Design Engineering Technical Conferences & Computers and Information in Engineering Conference, Washington, D.C., Aug 29-31, 2011. DETC2011-47402, (2011).

www.manaraa.com

[67] Zhou, Z., Wang, H., You, Z., "A Method of Designing Developable Origami Structures in Three-Dimensional Space – Part A: Mathematical Foundation" in Proceedings of the ASME 2014 International Design Engineering Technical Conferences & Computers and Information in Engineering Conference, Buffalo, New York, Aug 17-20, 2014. DETC2014-34588, (2014).

[68] Jin, M., Zhang, X., Zhu, B., "Design of Compliant Mechanisms Using A Pseudo-Rigid-Body Model Based Topology Optimization Method" in Proceedings of the ASME 2014 International Design Engineering Technical Conferences & Computers and Information in Engineering Conference, Buffalo, New York, Aug 17-20, 2014. DETC2014-34325, (2014).

[69] Zhao, K., Schmiedeler, J.P., "Using Rigid-Body Mechanism Topologies to Design Shape-Changing Compliant Mechanisms" in Proceedings of the ASME 2013 International Design Engineering Technical Conferences & Computers and Information in Engineering Conference, Portland, Oregon, Aug 4-7, 2013. DETC2013-12576, (2013).

[70] Zirbel, S.A., Magleby, S.P., Howell, L.L., Lang, R.J., Thomson, M.W., Sigel, D.A., Walkemeyer, P.E., Trease, B.P., "Accommodating Thickness in Origami-Based Deployable Arrays" in Proceedings of the ASME 2013 International Design Engineering Technical Conferences & Computers and Information in Engineering Conference, Portland, Oregon, Aug 4-7, 2013. DETC2013-12348., (2013)

[71] Francis, K. C., Rupert, L. T., Lang, R. J., Morgan, D. C., Magleby, S. P., Howell, L. L., "From Crease Patter to Product: Considerations to Engineering Origami-Adapted Designs" in Proceedings of the ASME 2014 International Design Engineering Technical Conferences & Computers and Information in Engineering Conference, Buffalo, New York, Aug 17-20, 2014. DETC-2014-34031, (2014).

[72] Radaelli, G., Herder, J. L., "Isogeometric Shape Optimization for Compliant Mechanisms With Prescribed Load Paths" in Proceedings of the ASME 2014 International Design Engineering Technical Conferences & Computers and Information in Engineering Conference, Buffalo, New York, Aug 17-20, 2014. DETC-2014-35373, (2014).

[73] Ugray, Zsolt, Leon Lasdon, John C. Plummer, Fred Glover, James Kelly, and Rafael Martí. "Scatter Search and Local NLP Solvers: A Multistart Framework for Global Optimization." INFORMS Journal on Computing, Vol. 19, No. 3, pp. 328–340, (2007).

[74] Katz, A., Lusk, C., "Design of an Origami Fold Pattern for Shape-Morphing Using Triangles" in Proceedings of the ASME 2016 International Design Engineering Technical Conference & Computers and Information in Engineering Conference, Charlotte, NC, Aug. 21-24, 2016. DETC2016-59604, (2016).

المنارة للاستشارات
www.manaraa.com

[75] Alqasimi, A., Lusk, C., “Shape-Morphing Space Frame (SMSF) Using Linear Bistable Elements” in Proceedings of the ASME 2015 International Design Engineering Technical Conference & Computers and Information in Engineering Conference, Boston, MA, Aug. 2-5, 2015. DETC2015-47526, (2015).

[76] Hull, T., “On the mathematics of flat origamis” in Proceedings of the Twenty-fifth Southeastern International Conference on Combinatorics, Graph Theory and Computing, Boca Raton, FL, Congressus Numerantium 100, pp. 215-224, (1994).

[77] Kasahara, K., Takahama, T., *Origami for the Connoisseur*, New York: Japan Publications (1987).

[78] Kawasaki, T., “On the Relation Between Mountain-Creases and Valley-Creases of a Flat Origami” in Proceedings of the 1st International Meeting on Origami Science and Technology (Ed. H. Huzita), Ferrara, Italy, pp. 229-237, (1989).

[79] Justin, J., “Aspects mathematiques du pliage de papier”, In Proceedings of the First International Meeting of Origami Science, Mathematics, and Education, edited by Thomas Hull, pp. 29-37. Natick, MA: A K Peters, (2002).

[80] Lu, Y., Mao, B., Yu, J., “Derivation and isomorphism identification of valid topological graphs for 1-, 2-DOF planar closed mechanisms by characteristic strings”, Journal of Mechanical Science and Technology 25 (1) 255~263, DOI: 10.1007/s12206-010-1201-y, (2011).

[81] Bowen, L. A., Grames, C. L., Magleby, S. P., Howell, L. L., Lang, R. J., “A Classification of Action Origami as Systems of Spherical Mechanisms” Journal of Mechanical Design, November, Vol. 135, 111008, (2013).

[82] Miura, K., “Method of packaging and deployment of large membranes in space”, Tech. Report 618, The Institute of Space and Astronautical Science (1985).

[83] Katz, A., Nussbaum, J., Crane, N. B., Lusk, C. P., “Stress-Limiting Test Structures For Rapid Low-Cost Strength and Stiffness Assessment” Rapid Prototyping Journal, Vol. 21, Iss. 2, pp. 144-151, (2015).

[84] Gibson, I., Rosen D. W., and Stucker, B., *Additive Manufacturing Technologies: Rapid Prototyping to Direct Digital Manufacturing.* New York: Springer, (2010).

[85] Abe, F., Costa Santos E., Kitamura, Y., Osakada K., and Shiomi, M., "Influence of forming conditions on the titanium model in rapid prototyping with the selective laser melting process," Proc. Inst. Mech. Eng. Part C, Vol. 217, pp. 119-126, (2003).

[86] Ahn S., Montero, M., Odell, D., Roundy S., and Wright, P. K., "Anisotropic material properties of fused deposition modeling ABS," Rapid Prototyping Journal, Vol. 8, pp. 248-257, (2002).

www.manaraa.com

[87] Hossain, M. S., Ramos, J., Espalin, D., Perez M., and Wicker, R., "Improving tensile mechanical properties of FDM-manufactured specimens via modifying build parameters," in Solid Fabrication Symposium, Austin, TX, (2013).

[88] Kulkarni P., Dutta, D., "Deposition strategies and resulting part stiffnesses in fused deposition modeling," J. Manuf. Sci. Eng. Trans. ASME, Vol. 121, pp. 93-103, (1999).

[89] Thrimurthulu, K., Pandey P. M., Reddy, N. V., "Optimum part deposition orientation in fused deposition modeling," International Journal of Machine Tools & Manufacture, vol. 44, pp. 585-94, 05, (2004).

[90] Cooper, K. P., Wachter, R. F., "On making additive manufacturing a production technology", pp. 1593, (2011).

[91] Xiong, J., Zhang, G., "Online Measurement of bead Geometry in Gmaw-based Additive Manufacturing Using Passive Vision," Vol. 24, pp. 115103 (7 pp.), 11, (2013).

[92] Zeng, K., Patil, N., Gu, H., Gong, H., Pal, D., Starr, T., Stucker, B., "Layer by layer validation of geometrical accuracy in additive manufacturing processes," in 24th International Solid Freeform Fabrication Symposium - an Additive Manufacturing Conference, August 12 - 14, pp. 76-87, (2013).

[93] Akhter, N., Jung, H., Chang, H., Kim, K., "Determination of elastic modulus of a beam by using electronic speckle pattern interferometry" Opt. Laser Technol., Vol. 41, pp. 526-529, (2009).

[94] Digilov, R. M., "Flexural vibration test of a cantilever beam with a force sensor: fast determination of Young's modulus," European Journal of Physics, vol. 29, pp. 589-97, 05, (2008).

[95] Digilov, R. M., Abramovich, H., "Flexural Vibration Test of a Beam Elastically Restrained at One End: A New Approach for Young's Modulus Determination," Advances in Materials Science & Engineering, pp. 329530 - 329536, (2013).

[96] ASTM Standard E1876-01, "Standard test method for dynamic young's modulus, shear modulus, and Poisson's ratio by impulse excitation of vibration," ASTM International, West Conshohocken, PA, (2006).

[97] R. J. Roark, W. C. Young, *Roark's Formulas for Stress and Strain.* New York: McGraw-Hill.

[98] APSplus-P430 http://www.stratasys.com/~/media/Main/Secure/Material%20Specs%20MS/Fortus-Material-Specs/Fortus-MS-ABSplus-01-13-web.pdf. (2014).

المنارة للاستشارات

www.manaraa.com

[99] Raut, S. V., Jatti, V. S., Singh, T. P., "Influence of built orientation on mechanical properties in fused deposition modeling," in 2014 International Mechanical Engineering Congress, June 13 – 15, pp. 400-404, (2014).

[100] Dimension P400 Material Properties [Dimension P400 Material Properties]. Available: https://store.amtekcompany.com/products.php?product=Dimension-Standard-ABS-Model-Material-%25252d-P400.

المنارة للاستشارات

www.manaraa.com

APPENDIX A: COPYRIGHT PERMISSIONS

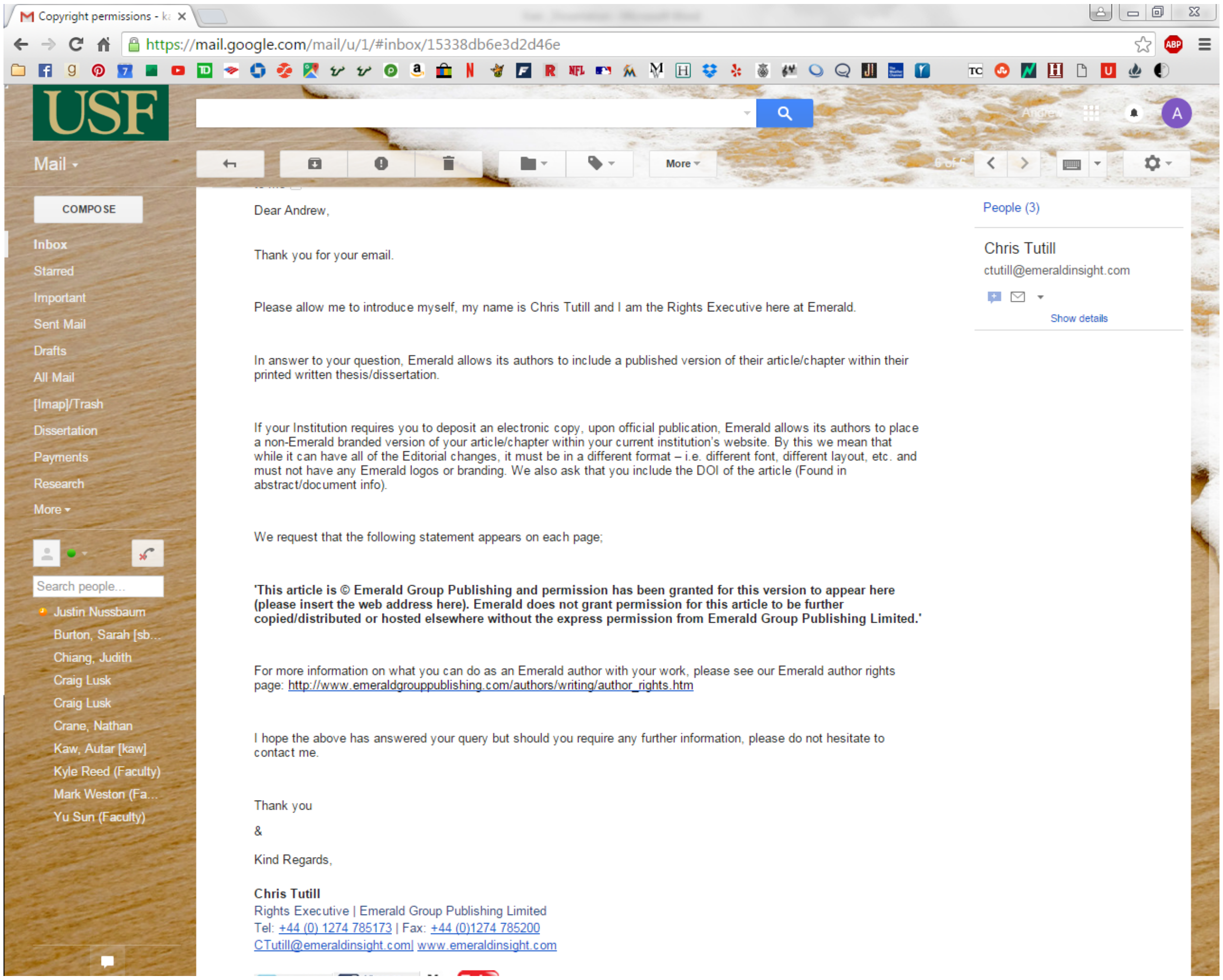

Dear Andrew,

Thank you for your email.

Please allow me to introduce myself, my name is Chris Tutill and I am the Rights Executive here at Emerald.

In answer to your question, Emerald allows its authors to include a published version of their article/chapter within their printed written thesis/dissertation.

If your Institution requires you to deposit an electronic copy, upon official publication, Emerald allows its authors to place a non-Emerald branded version of your article/chapter within your current institution's website. By this we mean that while it can have all of the Editorial changes, it must be in a different format – i.e. different font, different layout, etc. and must not have any Emerald logos or branding. We also ask that you include the DOI of the article (Found in abstract/document info).

We request that the following statement appears on each page;

'This article is © Emerald Group Publishing and permission has been granted for this version to appear here (please insert the web address here). Emerald does not grant permission for this article to be further copied/distributed or hosted elsewhere without the express permission from Emerald Group Publishing Limited.'

For more information on what you can do as an Emerald author with your work, please see our Emerald author rights page: http://www.emeraldgrouppublishing.com/authors/writing/author_rights.htm

I hope the above has answered your query but should you require any further information, please do not hesitate to contact me.

Thank you

&

Kind Regards,

Chris Tutill
Rights Executive | Emerald Group Publishing Limited
Tel: +44 (0) 1274 785173 | Fax: +44 (0)1274 785200
CTutill@emeraldinsight.com| www.emeraldinsight.com

The above image is an email from Emerald Group Publishing Rights Representative, Chris Tutill, explaining how Emerald Group papers should be used in a dissertation. This gives permission for the use of content in Chapter 4.

المنارة للاستشارات
www.manaraa.com

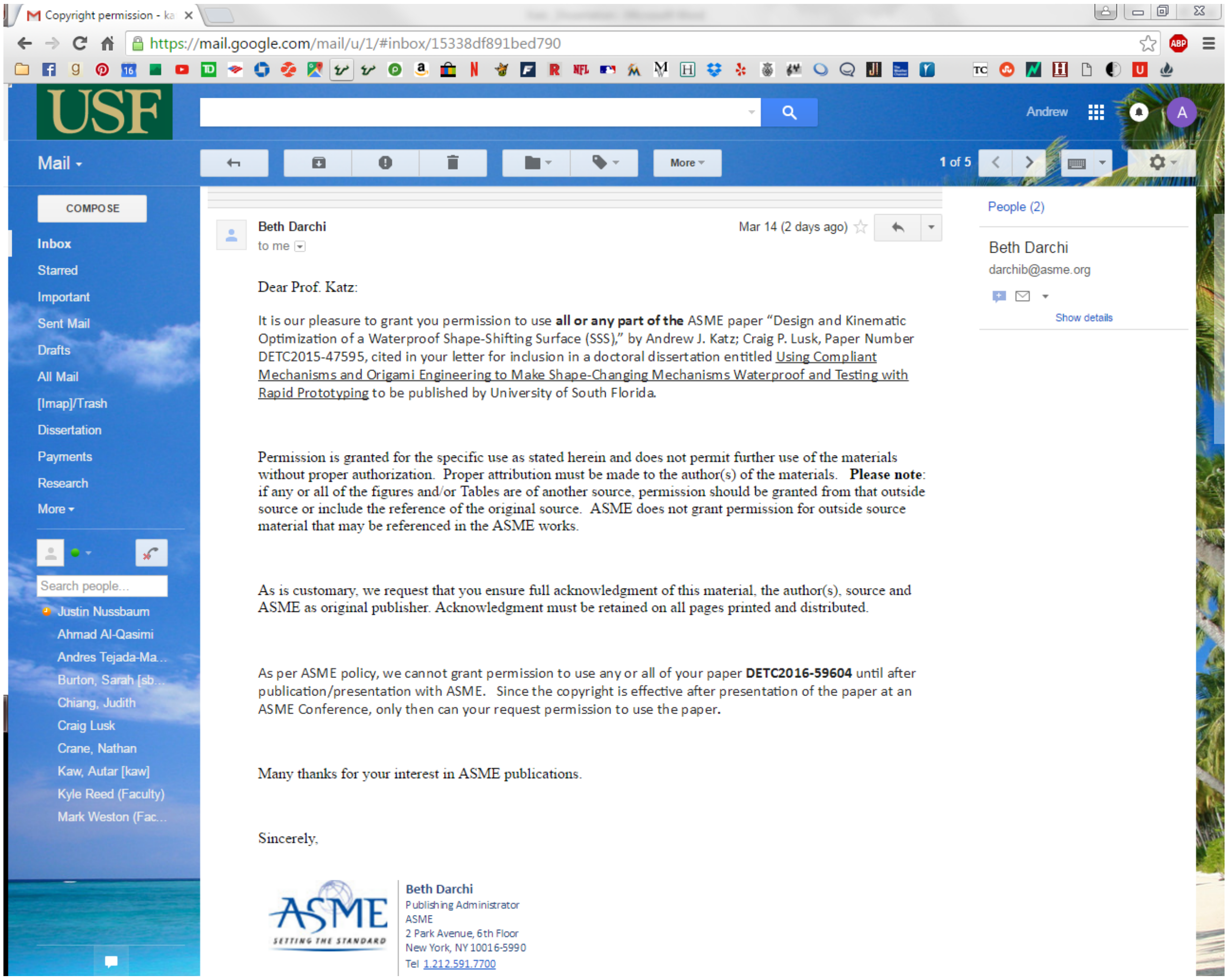

Beth Darchi
to me

Mar 14 (2 days ago)

Dear Prof. Katz:

It is our pleasure to grant you permission to use **all or any part of the** ASME paper "Design and Kinematic Optimization of a Waterproof Shape-Shifting Surface (SSS)," by Andrew J. Katz; Craig P. Lusk, Paper Number DETC2015-47595, cited in your letter for inclusion in a doctoral dissertation entitled Using Compliant Mechanisms and Origami Engineering to Make Shape-Changing Mechanisms Waterproof and Testing with Rapid Prototyping to be published by University of South Florida.

Permission is granted for the specific use as stated herein and does not permit further use of the materials without proper authorization. Proper attribution must be made to the author(s) of the materials. **Please note**: if any or all of the figures and/or Tables are of another source, permission should be granted from that outside source or include the reference of the original source. ASME does not grant permission for outside source material that may be referenced in the ASME works.

As is customary, we request that you ensure full acknowledgment of this material, the author(s), source and ASME as original publisher. Acknowledgment must be retained on all pages printed and distributed.

As per ASME policy, we cannot grant permission to use any or all of your paper **DETC2016-59604** until after publication/presentation with ASME. Since the copyright is effective after presentation of the paper at an ASME Conference, only then can your request permission to use the paper.

Many thanks for your interest in ASME publications.

Sincerely,

ASME
SETTING THE STANDARD

Beth Darchi
Publishing Administrator
ASME
2 Park Avenue, 6th Floor
New York, NY 10016-5990
Tel 1.212.591.7700

The above image is an email from ASME Publishing Rights Administrator, Beth Darchi, explaining how ASME papers should be used in a dissertation. This gives permission for the use of content in Chapter 2.

المنارة للاستشارات
www.manaraa.com

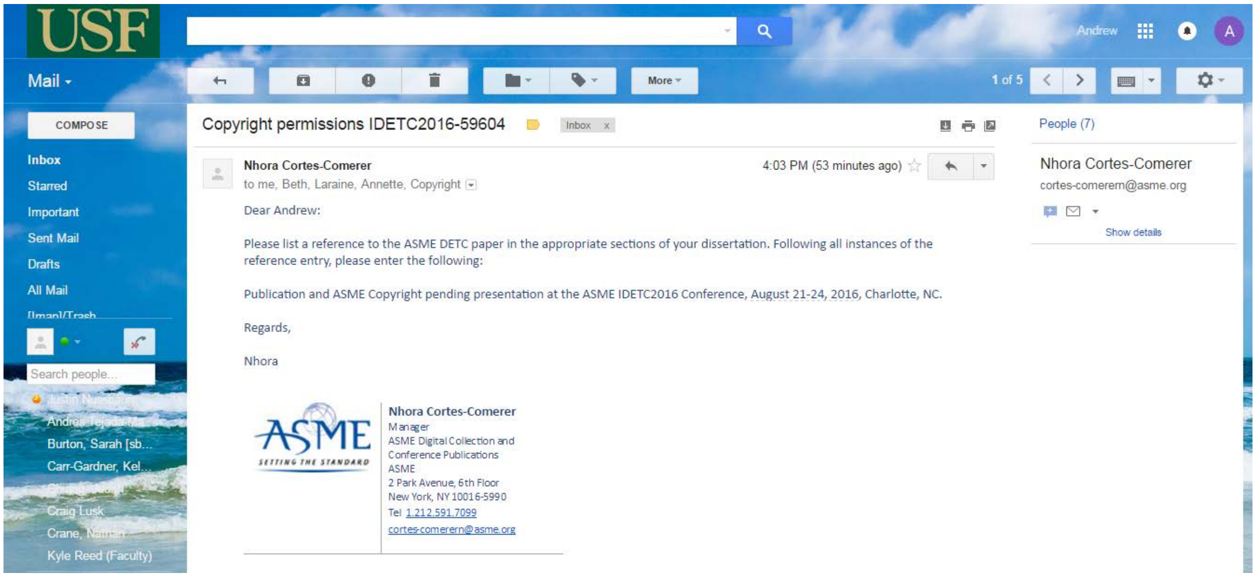

Copyright permissions IDETC2016-59604

Nhora Cortes-Comerer
to me, Beth, Laraine, Annette, Copyright
4:03 PM (53 minutes ago)

Dear Andrew:

Please list a reference to the ASME DETC paper in the appropriate sections of your dissertation. Following all instances of the reference entry, please enter the following:

Publication and ASME Copyright pending presentation at the ASME IDETC2016 Conference, August 21-24, 2016, Charlotte, NC.

Regards,

Nhora

ASME
SETTING THE STANDARD

Nhora Cortes-Comerer
Manager
ASME Digital Collection and
Conference Publications
ASME
2 Park Avenue, 6th Floor
New York, NY 10016-5990
Tel 1.212.591.7099
cortes-comerern@asme.org

Nhora Cortes-Comerer
cortes-comerern@asme.org

The above image is an email from ASME Manager, Nhora Cortes-Comerer, explaining how ASME papers should be used in a dissertation. This gives permission for the use of content in Chapter 3.

المنارة للاستشارات
www.manaraa.com

APPENDIX B: MATLAB CODE

The code outlined in appendix B is MATLAB code which ran two nested optimization routines, the purpose and details of which are described in Chapter 2.

B.1 Script That Calls The Outer Optimization

This code calls the outer optimization and defines the parameters of it.

```
%This script calls the optimization function along with all of its child
%functions
clc
%BEFORE RUNNING THE OPTIMIZATION MAKE SURE TO DELETE/MOVE/OR RENAME THE
%EXISTING FILES WHICH RECORD THE VARIABLE VALUES SO THAT THE NEW VALUES DO
%NOT MIX WITH THE OLD VALUES

%Utilizing the profile function will help to make the program run faster
%Starting point values for the optimization variables
x0 = [58.58 67.32 77.98 16.55 49.4 46.61 18.27];
x1 = [5.0636 6.1438 66.673 45.276 12.97 38.199 38.051];

%Lower bounds
lb = [0 0 0 0 0 0 0];

%Upper bounds
ub = [76.2 76.2 78 60.78 60.78 60.78 60.78];

%Used for testing the inneroptimization function
%in-neroptimization3(x0)

%Used for testing the whole optimization
%opt12code(x0,lb,ub)

%Specifies the options for the optimization problem
options = optimoptions('fmincon');
options = optimoptions(options,'Display', 'iter-detailed');
options = optimoptions(options,'OutputFcn', { @outputfun });
options = optimoptions(options,'PlotFcns', {  @optimplotx @optimplotfval
@optimplotfirstorderopt });
options = optimoptions(options,'Algorithm', 'interior-point');

%Defines the handle for the optimization setup
```

المنارة للاستشارات
www.manaraa.com

```
optimproblem =
createOptimProblem('fmincon','objective',@inneroptimization3,'x0',x0,'lb',lb,
'ub',ub,'nonlcon',@optconstraints,'options',options);

%Uses to search for a global optima
gs = GlobalSearch;
run(gs, optimproblem)

%Uses a multistart to search for global optima
%ms = MultiStart;
%run(ms, optimproblem, 20)

%Used to check the optimized design variables against the constraints
%function, the second to last number in the dlmread command is the
% desvar = dlmread('desvarvalues.txt');
% rc = size(desvar);
% x = desvar(rc(1),:)
% [C, Ceq] = optconstraints(x)
```

B.2 The Inner Optimization

This code uses a gradient based approach to solve the solid mechanis equations that dictate the behavior of the part.

```
function fyopt = inneroptimization3(x)
%This function solves the set of equations outlined in optfun and records
%the results in matrices, the bottom half of the function which is
%currently commented out checks the validity of the solutions by plotting
format shortg
%This is the necessary format for the inputs to this function
%Format: %x1 x2 x3 y1 y2 y3 y4
%x0 = [58.58 67.32 77.98 16.55 49.4 46.61 18.27]

%Design variables
%x's and y's are the final position of the given beam
%The first number is the coordinate in the CAD drawing, the number in
%parentheses is the coordinate in the hand drawing, the number after the
%colon is the variable as MATLAB recognizes it. The number in parentheses
%is the hand drawing and also the CAD drawing in the optimization folder.
% y1(x1): x(1) = -58.58;
% y2(x2): x(2) = -67.32;
% y3(x3): x(3) = -77.98;
% x1(y1): x(4) = 16.55; %r1 = 60.88
% x2(y2): x(5) = 49.4; %r2 = 33.997
% x3(y3): x(6) = 46.61; %r3 = 11.018
% x4(y4): x(7) = 18.27; %r4 = 28.57
% y4(x4): x(8) = -74.4;
% y5(x5): x(9) = -74.4;
% x5(y5): x(10) = 0;

%Order gets mixed up here because the inputs from the function must be
```

المنارة للاستشارات
www.manaraa.com

```
%x(1-7) so the only ones which I can prescribe are 8 9 and 10
%x(8) is really x4, x(9) is really x5, x(10) is really y5
x(8) = 74.4;
x(9) = 74.4;
x(10) = 0; %r5 = 18.529 (old value)

theta10 = atan((x(4)/x(1)));
theta20 = atan((x(5)-x(4))/(x(2)-x(1)));
theta30 = atan(-(x(6)-x(5))/(x(2)-x(3)));
theta40 = atan((x(7)-x(6))/(x(8)-x(3)))+pi;
theta50 = -pi/2;
t = [theta10 theta20 theta30 theta40 theta50];

r(1) = ((x(1)^2) + (x(4)^2))^0.5;
r(2) = (((x(2) - x(1))^2) + ((x(5) - x(4))^2))^0.5;
r(3) = (((x(3) - x(2))^2) + ((x(6) - x(5))^2))^0.5;
r(4) = (((x(8) - x(3))^2) + ((x(7) - x(6))^2))^0.5;
r(5) = (((x(9) - x(8))^2) + ((x(10) - x(7))^2))^0.5;
fid2 = fopen('lengths','w');
fwrite(fid2,r,'double');
fclose(fid2);

fid3 = fopen('angles','w');
fwrite(fid3,t,'double');
fclose(fid3);

%Input variables
%kk and range can be changed in order to help MATLAB solve the equations
%more easily, range must go back to its actual value, kk is just the number
%of steps and consequently the step size
kk = 10; %Number of iterations
range = 13.62; %Distance of actuation, original range is 13.62

indk = [0 0 t(2) t(3) t(4)]; %Inputs for the first stage optimization
solr(kk,5) = zeros;
FVAL1(kk,5) = zeros;
EXITFLAG(kk) = zeros;

for k = 1:kk
    varx = 74.4 - (range * ((1/kk) * (k-1))); %changes the distance which the
device is currently being actuated
    %Writes the aforementioned distance into a binary file to be read later
    %by the optimzation function, opteqns
    fid = fopen('var','w');
    fwrite(fid,varx,'double');
    fclose(fid);
    [sol1,FVAL,EXITFLAG(k)] =
(fsolve(@opteqns,indk,optimset('MaxFunEvals',2000,'FunValCheck','on','Display
','off')));
    %writes the results of the fsolve command into matrices
    for d = 1:5
        solr(k,d) = sol1(d);
        FVAL1(k,d) = FVAL(d);
    end
    indk = sol1;
```

www.manaraa.com

```
end

%Commented these out to try to make the program run faster, they are used
%to convert the angular variables to degrees from radians to make them
%easier to understand
%sold(:,3:5) = (solr(:,3:5)*180)/pi;
%sold(:,1:2) = (solr(:,1:2));
fyopt = mean(solr(:,2)) + max(abs(solr(:,2)));

%Everything past this line is used for checking the validity of the prior
%code

%solr((kk+1),:) = indk; %Checking the initial guess loop
% EXITFLAG
% solr
% sold
% FVAL1;

%Used to plot function values at each iteration
%for u = 1:5
    %plot(FVAL1(:,u))
    %pause
%end

%Verification test
% r(1) = 60.88;
% r(2) = 33.997;
% r(3) = 11.018;
% r(4) = 28.57;
% r(5) = 18.529;
% theta10 = (15.809 * pi) / 180; %0.2759 radians
% theta20 = (75.093 * pi)/ 180; %1.3106 radians
% theta30 = (345.331 * pi)/ 180; %6.0272
% theta40 = (262.802 * pi) /180; %4.5868
% theta50 = -pi/2;
%
% for q = 1:kk;
%     varx(q) = 74.4 - (13.62 * ((1/kk)*(q-1)));
%     %This line was at one point being used to check the initial guess loop
%     %varx(kk+1) = 74.4;
%     p1 = [0 + 1i*0];
%     p2 = p1 + [(r(1)*cos(theta10))+(1i*r(1)*sin(theta10))];
%     p3 = p2 + [(r(2)*cos(solr(q,3)))+(1i*r(2)*sin(solr(q,3)))];
%     p4 = p3 + [(r(3)*cos(solr(q,4)))+(1i*r(3)*sin(solr(q,4)))];
%     p5 = p4 + [(r(4)*cos(solr(q,5)))+(1i*r(4)*sin((solr(q,5))))];
%     p6 = p5 + [(r(5)*cos(theta50))+(1i*r(5)*sin(theta50))];
%     p7 = p6 - [varx(q)+1i*0];
%     z = [p1;p2;p3;p4;p5;p6;p7];
%     plot(real(z),imag(z))
%     hold on
%     %drawnow
%     pause
% end
end
```

www.manaraa.com

```
%a = 60.88
%b = 33.997
%c = 11.018
%d = 28.57
%e = 18.529

%t10 = 15.809
%t20 = 75.093
%t30 = 345.331
%t40 = 262.802
%t50 = 270
```

B.3 Optimization Constraints

This code defines the constraints of the optimization.

```
function [C, Ceq] = optconstraints(x)

%Inequality constraints
%Prevents any point from going outside of 3"
c1 = x(1) - 74.4;
c2 = x(2) - 74.4;
c3 = x(3) - 74.4;

%Shield cannot be larger than unit cell length minus actuation distance
%this allows the piece to be actuated without pieces sticking out of the
%actuated unit cell
%Keeps the center to right side length inside of 3"
c4 = x(4) - 60.78;
c5 = x(5) - 60.78;
c6 = x(6) - 60.78;
c7 = x(7) - 60.78;

%Keeps x2 in front of x1
c8 = x(1) - x(2);

%Equality constraints
%Keeps the top to bottom length at 3"
%Commented these out because I think it may have been incorrect
%c9 = x(4) - 74.4;
%c10 = x(5) - 74.4;

C = [c1; c2; c3; c4; c5; c6; c7; c8];
Ceq = [];
end
```

B.4 Inner Optimization Equations

This code defines the solid mechanics equations to be solved.

www.manaraa.com

```
function F = opteqns(ind)
%Andrew Katz
%Design optimization for shape shifting water proof surface

fid2 = fopen('lengths','r');
r = fread(fid2,'double');
fclose(fid2);

fid3 = fopen('angles','r');
t = fread(fid3,'double');
fclose(fid3);

psi2 = ind(3) - t(2);
psi3 = (ind(4) - t(3)) - (ind(3) - t(2));
psi4 = (ind(5) - t(4)) - (ind(4) - t(3));
psi5 = (ind(5) - t(4));
k2 = 2000; %have not yet accounted for I or L
k3 = 2000;
k4 = 2000;
k5 = 2000;

%Receives variables from the inneroptimization function
fid = fopen('var','r');
varx = fread(fid,'double');
fclose(fid);

F = [r(1)*cos(t(1)) + r(2)*cos(ind(3)) + r(3)*cos(ind(4)) + r(4)*cos(ind(5))
+ r(5)*cos(t(5)) - varx;...
r(1)*sin(t(1)) + r(2)*sin(ind(3)) + r(3)*sin(ind(4)) + r(4)*sin(ind(5)) +
r(5)*sin(t(5));...
(1/sin(ind(4) - ind(5))) * ((-k3*psi3*cos(ind(5))/r(3)) +
(k4*psi4*cos(ind(4))/r(4)) + (k4*psi4*cos(ind(5))/r(3)) +
(k5*psi5*cos(t(5))/r(4))) - ind(1);...
(1/(sin(ind(4) - ind(5)))) * ((k3*psi3*cos(t(5) - ind(5))/r(3)) +
(k4*psi4*cos(t(5) - ind(4))/r(4)) - ((k4*psi4*cos(t(5) - ind(5)))/r(3)) +
((k5*psi5*cos(t(5) - ind(5)))/r(3))) - ind(2);...
k2*psi2 + (k3*psi3*(((-r(2)*sin(ind(3) - ind(5)))/(r(3)*sin(ind(4) -
ind(5))))-1)) + (k4*psi4*((-r(2)*sin(ind(3) - ind(4)))/(r(4)*sin(ind(5) -
ind(4))))) - (k4*psi4*((r(2)*sin(ind(3) - ind(5)))/(r(3)*sin(ind(4) -
ind(5))))) + (k5*psi5*((-r(2)*sin(ind(3) - ind(4)))/(r(4)*sin(ind(5) -
ind(4)))))];
end

%ind(1) = Fx
%ind(2) = Fy
%ind(3) = theta2
%ind(4) = theta3
%ind(5) = theta4
%E(pp) = 1.5 - 2 GPa
```

www.manaraa.com

B.5 Output Function

This code records certain design variables to a separate file to be used at various times during the execution of the program.

```
function stop = outputfun(x, optimValues, state)
stop = false;

%Recording design variable results using a text file because the binary
%file is less convenient to read and because it rounds to the nearest
%integer and the text file rounds to the nearest hundreth
dlmwrite('desvarvalues.txt',x,'-append');

%Old code that attempted to save all plots in a multistart, never finished
%it because I wasn't sure that it was necessary
%h = gcf;
%saveas(h,'Plots')
end
```

المنارة للاستشارات
www.manaraa.com

APPENDIX C: CAD DRAWINGS FROM CHAPTER 2

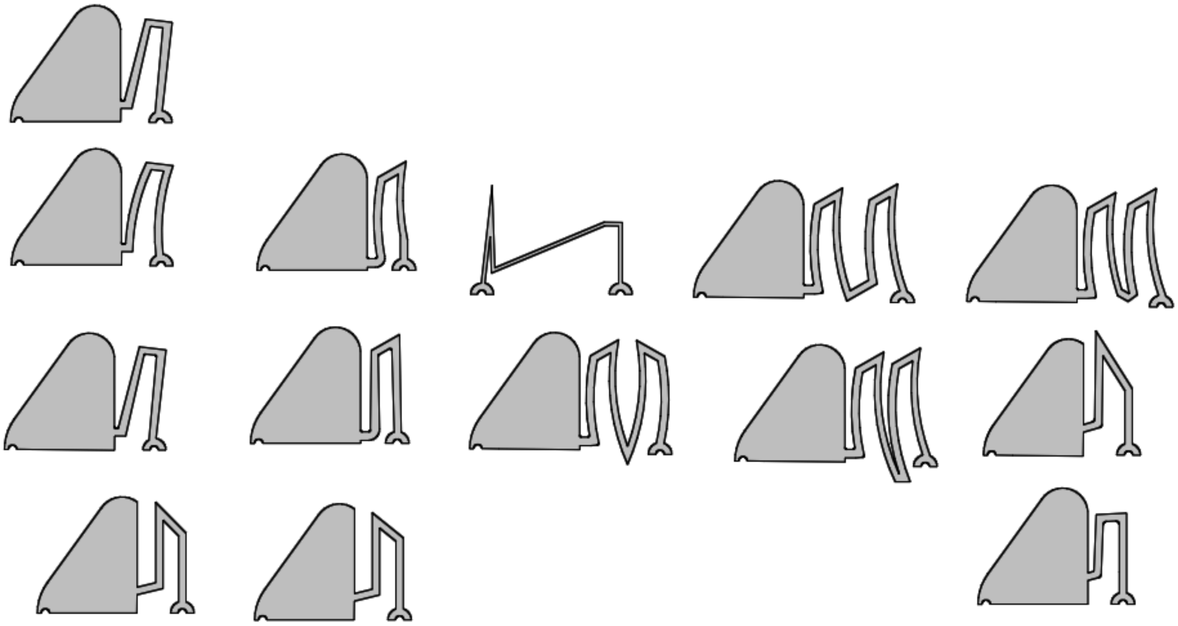

Figure C.1 These are various designs that were tested in Chapter 2 but were not deemed useful

www.manaraa.com

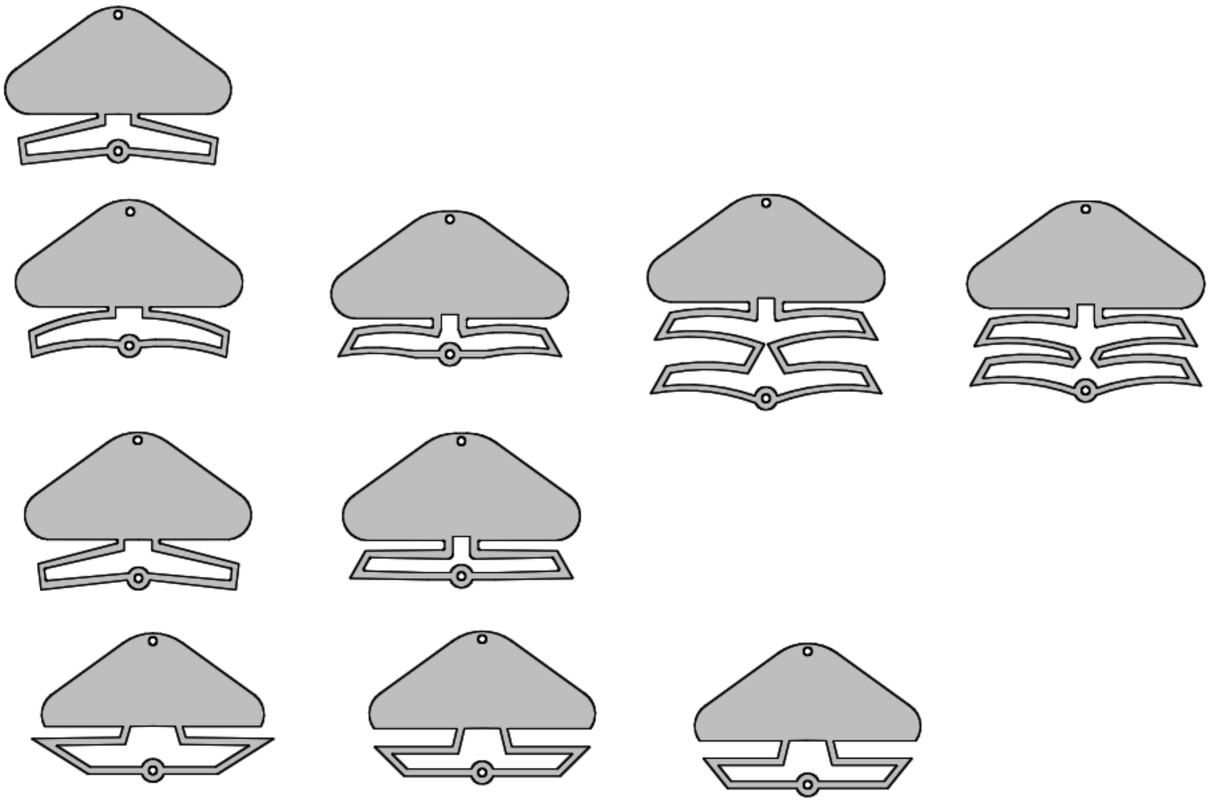

Figure C.2 These are various double size designs that were tested in Chapter 2 but were not deemed useful

www.manaraa.com

APPENDIX D: CAD DRAWINGS FROM CHAPTER 4

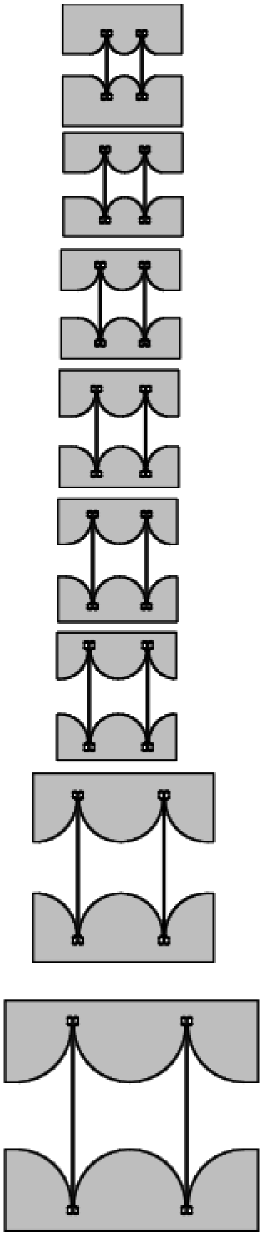

Figure D.1 These are all eight sizes of the part designed for Chapter 4

www.manaraa.com